

On the interplay between downwelling, deep convection and mesoscale eddies in the Labrador Sea

Georgiou, Sotiria; van der Boog, Carine G.; Brüggemann, Nils; Ypma, Stefanie L.; Pietrzak, Julie D.; Katsman, Caroline A.

DOI

[10.1016/j.ocemod.2019.02.004](https://doi.org/10.1016/j.ocemod.2019.02.004)

Publication date

2019

Document Version

Accepted author manuscript

Published in

Ocean Modelling

Citation (APA)

Georgiou, S., van der Boog, C. G., Brüggemann, N., Ypma, S. L., Pietrzak, J. D., & Katsman, C. A. (2019). On the interplay between downwelling, deep convection and mesoscale eddies in the Labrador Sea. *Ocean Modelling*, 135, 56-70. <https://doi.org/10.1016/j.ocemod.2019.02.004>

Important note

To cite this publication, please use the final published version (if applicable). Please check the document version above.

Copyright

Other than for strictly personal use, it is not permitted to download, forward or distribute the text or part of it, without the consent of the author(s) and/or copyright holder(s), unless the work is under an open content license such as Creative Commons.

Takedown policy

Please contact us and provide details if you believe this document breaches copyrights. We will remove access to the work immediately and investigate your claim.

On the interplay between downwelling, deep convection and mesoscale eddies in the Labrador Sea

Sotiria Georgiou^{a,*}, Carine G. van der Boog^a, Nils Brüggemann^b, Stefanie L. Ypma^a, Julie D. Pietrzak^a, Caroline A. Katsman^a

^a*Section of Environmental Fluid Mechanics, Faculty of Civil Engineering and Geosciences, Delft University of Technology, Delft, The Netherlands*

^b*Faculty of Mathematics, Informatics and Natural Sciences, University of Hamburg, Hamburg, Germany*

Abstract

In this study, an idealized eddy-resolving model is employed to examine the interplay between the downwelling, ocean convection and mesoscale eddies in the Labrador Sea and the spreading of dense water masses. The model output demonstrates a good agreement with observations with regard to the eddy field and convection characteristics. It also displays a basin mean net downwelling of 3.0 Sv. Our analysis confirms that the downwelling occurs near the west Greenland coast and that the eddies spawned from the boundary current play a major role in controlling the dynamics of the downwelling. The magnitude of the downwelling is positively correlated to the magnitude of the applied surface heat loss. However, we argue that this connection is indirect: the heat fluxes affect the convection properties as well as the eddy field, while the latter governs the Eulerian downwelling. With a passive tracer analysis we show that dense water is transported from the interior towards the boundary, predominantly towards the Labrador coast in shallow layers and towards the Greenland coast in deeper layers. The latter transport is steered by the presence of the eddy field. The outcome that the characteristics of the downwelling in a marginal sea like the Labrador Sea depend crucially on the properties of the eddy field emphasizes that it is essential to resolve the eddies to properly represent the downwelling and overturning in the North Atlantic Ocean, and its response to changing environmental conditions.

Keywords: deep convection, downwelling, mesoscale eddy, surface forcing, Labrador Sea, Atlantic Meridional Overturning Circulation

Preprint submitted to Ocean Modelling

December 18, 2018

1 Introduction

The Atlantic Meridional Overturning Circulation (AMOC) quantifies the zonally integrated meridional volume transport of water masses in the Atlantic Ocean. A prominent feature of the AMOC is an overturning cell where roughly 18 Sv ($1 \text{ Sv} = 10^6 \text{ m}^3 \text{ s}^{-1}$, [Cunningham et al. 2007](#); [Kanzow et al. 2007](#); [Johns et al. 2011](#)) of water flows northward above 1000 m, accompanied by a southward return flow at depth. As the surface waters flow northward through the Atlantic Ocean, they become dense enough to sink before they return southward at depth.

This lower limb of the AMOC contains water masses that can be traced back to specific deep ocean convection sites ([Marshall and Schott, 1999](#)). There are few regions in the world oceans where deep convection occurs, and numerous studies have revealed that the most important ones are in the marginal seas of the North Atlantic ([Dickson et al., 1996](#); [Lazier et al., 2002](#); [Pickart et al., 2002](#); [Eldevik et al., 2009](#); [Våge et al., 2011](#); [de Jong et al., 2012](#); [de Jong and de Steur, 2016b](#); [de Jong et al., 2018](#)).

Through the process of deep convection, dense waters are produced in the interior of the marginal seas, where the stratification is weak and the surface waters are exposed to strong heat losses ([Marshall and Schott, 1999](#)). While convection involves strong vertical transports of heat and salt, the interior of these marginal seas is known for a negligible amount of net downwelling. In particular, by applying the thermodynamic balance and vorticity balance to an idealized setting, [Spall and Pickart \(2001\)](#) pointed out that in a geostrophic regime, widespread downwelling in the interior of a marginal sea at high latitudes is unlikely, as it would have to be balanced by an unrealistically strong horizontal circulation. Instead, substantial downwelling of waters may occur along the perimeter of the marginal seas where the geostrophic dynamical constraints do not hold.

Using an idealized model, [Spall \(2004\)](#) demonstrated that significant downwelling indeed only occurs at the topographic slopes of a marginal sea subject to buoyancy loss. This downward motion yields an ageostrophic vorticity balance in which the vertical stretching term and lateral diffusion term near the boundary dominate ([Spall, 2010](#)). [Straneo \(2006b\)](#) considered the downwelling near the boundary from a different perspective, by developing an analytical two-layer model. In this study, a convective basin

*Corresponding author: Sotiria Georgiou, S.Georgiou@tudelft.nl, Environmental Fluid Mechanics, Stevingweg 1, 2628 CN, Delft, The Netherlands

36 is represented by two regions; the interior, where dense water formation
37 occurs due to surface buoyancy loss, and a buoyant boundary current that
38 flows around the perimeter of the marginal sea. It is assumed that instabil-
39 ities provide the lateral advection of buoyancy from the cyclonic boundary
40 current towards the interior required to balance the atmospheric buoyancy
41 loss over the interior. This alongstream buoyancy loss of the boundary cur-
42 rent reduces the density difference between the boundary current and the
43 interior along the perimeter of the marginal sea. As a consequence, the
44 thermal wind shear of the boundary current decreases in downstream direc-
45 tion, and continuity then demands the water to downwell at the coast (see
46 also [Katsman et al. \(2018\)](#) and references therein).

47 [Spall and Pickart \(2001\)](#) argue that the magnitude of the buoyancy loss
48 of the boundary current determines the amount of downwelling that occurs
49 near the boundary. While the surface buoyancy loss contributes to this
50 buoyancy loss, it is assumed to be mainly driven by eddies generated by
51 instabilities of the boundary current ([Spall, 2004](#); [Straneo, 2006b](#)).

52 Eddies shed from the boundary current also play an important role for
53 the cycle of ocean convection and restratification. Deep convection occurs
54 during wintertime in the southwest Labrador Sea ([Clarke and Gascard,
55 1983](#); [Lavender et al., 2000](#); [Pickart et al., 2002](#); [Våge et al., 2008](#)). The
56 dense water that is formed during the convection events, Labrador Sea Wa-
57 ter (LSW), strongly contributes to the structure of the North Atlantic Deep
58 Water, which in turn is a crucial component of the AMOC ([Lazier et al.,
59 2002](#); [Yashayaev et al., 2007](#); [Pickart and Spall, 2007](#); [Lozier, 2012](#)). Several
60 studies show that the thermohaline characteristics of LSW are influenced
61 not only by external parameters like the surface heat fluxes, but also by
62 the baroclinic structure of the boundary current that enters the Labrador
63 Sea ([Spall, 2004](#); [Straneo, 2006a](#)), known as the West Greenland Current
64 (WGC), and its interannual variability ([Rykova et al., 2015](#)).

65 In the Labrador Sea heat is carried from the WGC into the interior by
66 Irmingier Rings (IRs): large mesoscale eddies that are formed off the west
67 coast of Greenland in a region characterized by a steep topographic slope
68 ([Lilly et al., 2003](#); [Katsman et al., 2004](#); [Bracco et al., 2008](#); [Gelderloos
69 et al., 2011](#)). It has been recognised that the IRs strongly contribute to
70 compensating the annual mean heat loss to the atmosphere that occurs in
71 the Labrador Sea ([Katsman et al., 2004](#); [Hátún et al., 2007](#); [Kawasaki and
72 Hasumi, 2014](#)).

73 From the above, it is clear that eddies are of immense significance for

74 the downwelling as well as for the convection and the heat budget in the
75 Labrador Sea. The dynamics of the downwelling and how it is related to
76 the observed export of dense water masses is a topic of ongoing research,
77 as the quantitative effects of the interplay between downwelling, eddies and
78 convection are far from clear. For example, in a basin subject to buoyancy
79 loss, one expects that an increase of the heat loss will result in denser
80 and most likely deeper mixed layers. At first glance, this will increase
81 the horizontal density gradients within the basin, strengthen the baroclinic
82 instability of the boundary current and hence intensify the eddy field and
83 the strength of the downwelling. This suggests a positive feedback of the
84 increased eddy fluxes on the downwelling. However, the enhanced efficiency
85 of eddies to restratify the interior after convection may provide a negative
86 feedback on the convection and it is not clear a priori what the net effect
87 will be.

88 Moreover, observations show that convected waters that originate from
89 the Labrador Sea contribute to the lower limb of the AMOC (Rhein et al.,
90 2002; Bower et al., 2009). This suggests that there has to be a connection
91 between the convective regions (where these dense waters are formed) and
92 the surrounding circulation near the boundary (where waters can sink) that
93 has not been fully explored. Eddies provide a possible natural connection
94 between these two regions.

95 The aim of this study is to assess the quantitative impacts of the eddy
96 field on the downwelling in the Labrador Sea and its interaction with deep
97 convection. We seek to gain more insight in the dynamics that control
98 the downwelling in a convective marginal sea and its response to changing
99 forcing conditions. Towards this goal, we use a highly idealized configuration
100 of a high-resolution regional model in order to isolate specific processes
101 and connect the outcomes with theory. In particular, we diagnose how
102 the eddy field influences the downwelling by exchanging heat between a
103 warm boundary current and a cold interior basin subject to convection.
104 We compare our results to previous theories of downwelling dynamics. In
105 addition, we use a passive tracer study to shed light into the pathways
106 of the dense water masses and especially focus on the role of the eddies
107 in determining these pathways. Finally, by using two sensitivity studies
108 reflecting a milder and colder winter climate state, we test the sensitivity
109 of the downwelling and the export of dense waters with regard to varying
110 surface forcing.

111 The paper is organized as follows: the model setup and the simulations

112 performed are described in [section 2](#). The representation of deep convection
113 and the characteristics of the downwelling are described in [section 3](#). The
114 response of the deep convection and the time mean downwelling to changes
115 in the surface forcing is presented in [section 4](#), followed by a discussion in
116 [section 5](#). The conclusions of this work are presented in [section 6](#).

117 **2. Model setup**

118 *2.1. Model domain and parameters*

119 The numerical simulations performed in this study are carried out using
120 the MIT general circulation model ([Marshall et al., 1997](#)) in an idealized con-
121 figuration for the Labrador Sea. MITgcm solves the hydrostatic primitive
122 equations of motion on a fixed Cartesian, staggered C-grid in the horizontal.
123 The configuration of the model is an improved version of the one used in
124 the idealized studies of [Katsman et al. \(2004\)](#) and [Gelderloos et al. \(2011\)](#),
125 which now incorporates seasonal variations of both the surface forcing and
126 the boundary current and enhanced vertical resolution.

127 The model domain is 1575 km in the meridional direction and 1215 km
128 in the zonal direction. It has a horizontal resolution of 3.75 km in x and y
129 direction ([Fig. 1a](#)), which is below the internal Rossby radius of deformation
130 for the first baroclinic mode in the Labrador Sea (~ 7.5 km, [Gascard and
131 Clarke 1983](#)). The model has 40 levels in the vertical with a resolution of 20
132 m in the upper layers up to 200 m near the bottom. The maximum depth
133 is 3000 m and a continental slope is present along the northern and western
134 boundaries ([Fig. 1a](#)). Following [Katsman et al. \(2004\)](#) and [Gelderloos et al.
135 \(2011\)](#), we apply a narrowing of the topography to mimic the observed
136 steepening of the slope along the west coast of Greenland, which is crucial
137 for the shedding of the IRs from the boundary current ([Fig. 1a](#), [Bracco
138 et al. 2008](#)). The continental shelves are not included. There are two
139 open boundaries (each roughly 100 km wide), one in the east and one in
140 the southwest, where the prescribed boundary current enters and exits the
141 domain. All the other boundaries are closed ([Fig. 1a](#)).

142 Subgrid-scale mixing is parameterized using Laplacian viscosity and dif-
143 fusivity in the vertical direction and biharmonic viscosity and diffusivity
144 in the horizontal direction. The horizontal and vertical eddy viscosity
145 are $A_h = 0.25 \times 10^9 \text{ m}^4 \text{ s}^{-1}$ and $A_v = 1.0 \times 10^{-5} \text{ m}^2 \text{ s}^{-1}$ respectively, while
146 the horizontal diffusion coefficient is $K_h = 0.125 \times 10^9 \text{ m}^4 \text{ s}^{-1}$. The ver-
147 tical diffusion coefficient is described by a horizontally constant profile
148 which decays exponentially with depth as $K_v(z) = K_b + K_0 \times e^{(-z/z_b)}$, where

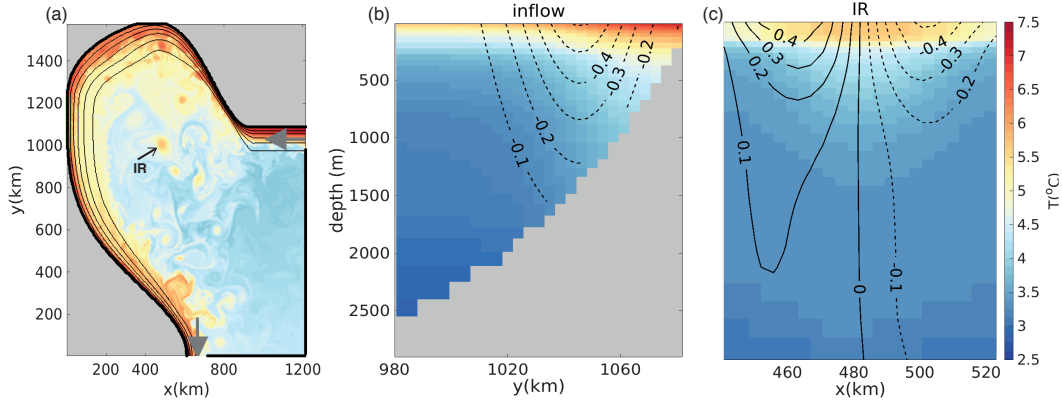


Fig. 1: (a) Snapshot of the sea surface temperature (SST) for the reference simulation (referred to in the text as REF). Black contours outline the bathymetry, the contour interval is 500 m starting from the isobath of 500 m. The grey arrows represent the inflow/outflow, where the boundaries are open ($x_{\text{inflow}} = 1215$ km, $y_{\text{inflow}} = 978.75 - 1083.75$ km and $x_{\text{outflow}} = 611.25 - 708.75$ km, $y_{\text{outflow}} = 3.75$ km) (b) Section across the inflow region (at $x = 1215$ km) showing the annual mean temperature (T_{in} , in $^{\circ}\text{C}$) and meridional velocity (U_{in} , in m s^{-1} , black contours). (c) Zonal section of an example Irminger Ring in the REF simulation by means of temperature (shading, in $^{\circ}\text{C}$) and meridional velocity (black contours, in m s^{-1}). This Irminger Ring is visible in the SST snapshot in the basin interior ($x=443-525$ km and $y=1012.5$ km) in (a).

149 $K_b = 10^{-5} \text{ m}^2 \text{ s}^{-1}$, $K_0 = 10^{-3} \text{ m}^2 \text{ s}^{-1}$ and $z_b = 100$ m. Temperature is
 150 advected with a quasi-second order Adams-Bashforth scheme. In case of
 151 statically unstable conditions, convection is parameterized through enhanced
 152 vertical diffusivity ($K_v = 10 \text{ m}^2 \text{ s}^{-1}$). A linear bottom drag with coefficient
 153 $2 \times 10^{-4} \text{ m s}^{-1}$ is applied.

154 Following Katsman et al. (2004), the model is initialized with a spatially
 155 uniform stratification, $\rho_{\text{ref}}(z)$, representative of the stratification in the west-
 156 ern Labrador Sea in late summer along the WOCE AR7W section. Only
 157 temperature variations are considered in the model, so this stratification is
 158 represented by a vertical gradient in temperature, $T_{\text{ref}}(z)$, calculated from
 159 $\rho_{\text{ref}}(z)$ using a linear equation of state: $\rho_{\text{ref}}(z) = \rho_0[1 - \alpha (T - T_{\text{ref}}(z))]$,
 160 where $\rho_0 = 1028 \text{ kg m}^{-3}$ and α the thermal expansion coefficient ($\alpha = 1.7 \times 10^{-4} \text{ }^{\circ}\text{C}^{-1}$).

161 The effects of salinity are not incorporated in the model. In reality,
 162 salinity does affect the properties of deep convection in the Labrador Sea,
 163 as the IRs shed from the boundary current carry cold, fresh shelf waters at
 164 their core (e.g., Lilly and Rhines, 2002; de Jong et al., 2016a). As shown in
 165 for example Straneo (2006a) and Gelderloos et al. (2012), the contribution

166 of this lateral fresh water flux to the buoyancy of the Labrador Sea interior
167 impacts the convection depth, and large salinity anomalies may in fact be
168 partly responsible for observed episodes when deep convection shut down
169 (Belkin et al., 1998; Dickson et al., 1988). However, since we focus here on
170 the underlying dynamics that control the downwelling and its response to
171 changing forcing conditions, the effects of salinity are omitted in the model
172 for simplicity.

173 *2.2. Model forcing*

174 At the eastern open boundary, an inflow representing the WGC is speci-
175 fied by a meridional temperature field $T_{\text{in}}(y, z)$ and a westward flow $U_{\text{in}}(y, z)$
176 in geostrophic balance with this prescribed temperature (Katsman et al.,
177 2004). Although the WGC consists of cold, fresh Arctic-origin waters and
178 warm, salty waters from the Irminger Current (Fratantoni and Pickart,
179 2007) we only incorporate in the model density variations associated with
180 the latter part. The cool, fresh surface waters are omitted, since they
181 are found on the continental shelf, which is not included in our idealized
182 bathymetry (Fig. 1a). The time-mean structure of this warm boundary
183 current is shown in Fig. 1b. The boundary current follows the topography
184 and flows cyclonically around the basin. The seasonal variability of the
185 WGC seen in observations (Kulan and Myers, 2009; Rykova et al., 2015)
186 is represented in the model by adding a sinusoidal seasonally varying term
187 to the inflow conditions based on these observations ($\Delta U_{\text{max}} = 0.4 \text{ cm s}^{-1}$
188 that peaks in September and attains its minimum in March). At the south-
189 ern open boundary an Orlanski radiation condition (Orlanski, 1976) for
190 momentum and tracers is applied.

191 At the surface, only a temporally and spatially varying surface heat flux
192 is applied, which is an idealized version of the climatology of WHOI OAF flux
193 project (Yu et al., 2008). The strongest heat loss occurs on the northwestern
194 side of the basin (Fig. 2), and its amplitude decays linearly away from this
195 heat loss maximum (white marker in Fig. 2b). The net annual heat loss
196 over the entire model domain of the reference simulation (hereinafter REF)
197 is -18 W m^{-2} . The time dependence of the amplitude of the surface heat
198 fluxes (Fig. 2c) is also based on the observations, ranging from -320 W m^{-2}
199 (January) to 140 W m^{-2} (July) at the location of the heat loss maximum.

200 One of the main objectives of this study is to investigate how changes
201 in the surface heat fluxes influence the evolution of convection, eddy ac-
202 tivity and the magnitude of the downwelling. For this reason, we perform

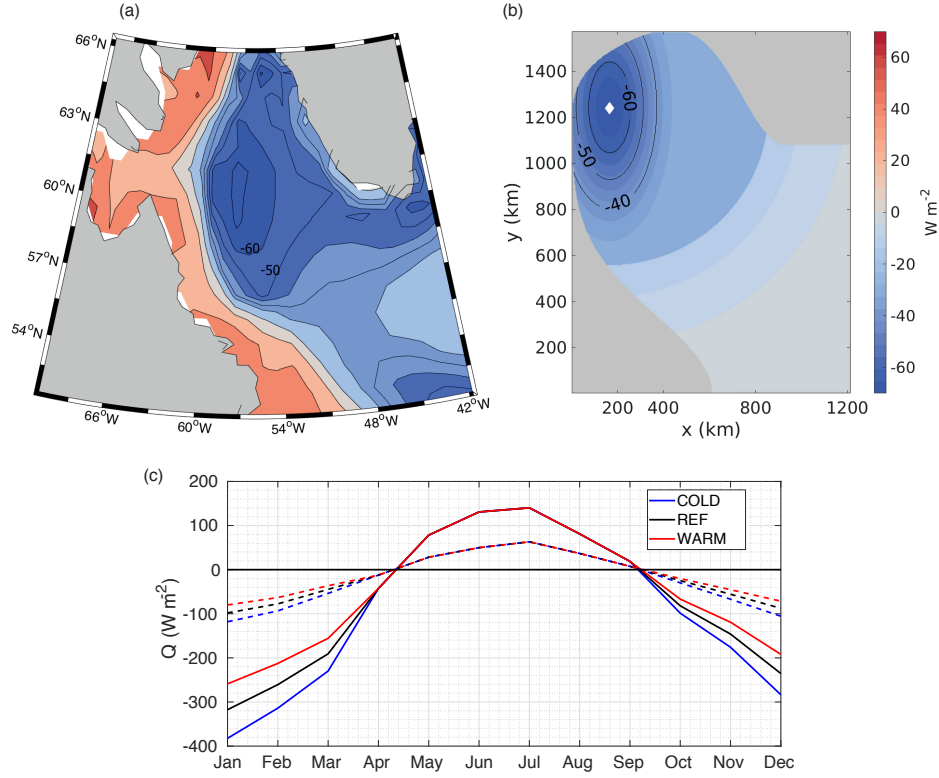


Fig. 2: (a) 1983-2009 mean of heat flux from the climatology of WHOI OAFflux project (Yu et al., 2008). (b) Annual mean surface heat flux applied to the model. $Q < 0$ means cooling of the sea surface, Q in $W m^{-2}$. (c) Seasonal cycle of the amplitude of the heat flux at the location where the amplitude is maximum (white marker in b, solid lines) and the mean over the basin (dashed lines) for the three different simulations (black: REF, red: WARM and blue: COLD).

203 sensitivity studies, in which we change the atmospheric cooling in winter-
 204 time by 50% with respect to the reference simulation (Fig. 2c). The net
 205 annual heat loss over the entire model domain for these simulations with a
 206 colder and warmer wintertime regime (hereinafter COLD and WARM) is
 207 -25 and $-12 W m^{-2}$ respectively or a 33% increase (28% decrease) in heat
 208 loss with respect to REF. In agreement with Gelderloos et al. (2012) and
 209 Moore et al. (2012), the mean winter heat loss (December-February, at the
 210 location of the heat loss maximum) is between -170 to $-250 W m^{-2}$ in these
 211 simulations.

212 *2.3. Model simulations*

213 All the simulations are performed for a period of 20 years in which each
214 model year is defined as 12 months with 30 days each for simplicity. The
215 2-day snapshots and the monthly means of all diagnostics are stored. For
216 our analysis, we use the snapshots from the last five years of the simulations
217 phase (i.e. model years 16 to 20).

218 Earlier studies have identified three types of eddies that may play a
219 role for the dynamics of the Labrador Sea (Chanut et al., 2008; Gelderloos
220 et al., 2011; Thomsen et al., 2014): the large Irminger Rings (IR) shed
221 near the west coast of Greenland, convective eddies (CE) and boundary
222 current eddies (BCE) that arise on fronts surrounding the convection region
223 in winter and on the front between the boundary current and the interior,
224 respectively. The latter two typically have a scale on the order of the Rossby
225 deformation radius, and are much smaller than the IRs. At a resolution of
226 3.75 km we barely resolve these mesoscale CE and BCE. However, the IR
227 are well represented in our model simulations.

228 A snapshot of the sea surface temperature for REF (Fig. 1a) illustrates
229 that in the idealized model, warm core IRs are formed at the west coast of
230 Greenland, where the slope is steep. A cross section of a representative IR is
231 shown in Fig. 1c. The maximum velocity in the IR ranges between 0.5 and
232 0.8 m s⁻¹ and the radius is approximately 30 km. This is in line with the
233 observational studies of Lilly et al. (2003) and de Jong et al. (2014) who find
234 maximum velocities between 0.3 to 0.8 m s⁻¹ and diameters of 30-60 km.
235 The temperature anomaly at the core of the modelled IR (representative
236 of its buoyancy anomaly; recall that salinity effects are omitted) reaches at
237 1500 m. Moreover, the average temperature between 200 and 1000 m is
238 4.25 °C, which is in good agreement with the observed vertical structure of
239 IRs as characterized by de Jong et al. (2014).

240 Fig. 3a shows the timeseries of the basin-mean temperature for the sim-
241 ulations. The impact of the seasonal cycle of the applied surface heat flux
242 is evident. For all the simulations, after ~ 10-15 years of integration the
243 basin-mean temperature reaches a quasi-equilibrium. In this model, such
244 an equilibrium can only be reached if the lateral advection of heat efficiently
245 balances the heat that is lost to the atmosphere. A heat budget analysis
246 indicates that this idealized model can reproduce the balance between the
247 lateral heat advection and the surface heat flux (Fig. 3b and 3c), as proposed
248 by Straneo (2006b) and Spall (2012). Although the mean heat advection
249 and the eddy heat advection mostly cancel each other (Fig. 3d and Fig. 3e),

250 the eddy heat advection dominates in the interior while the heat advection
251 by the mean flow dominates within the boundary current. The eddy heat
252 advection clearly shows the expected transport from the boundary to the
253 interior (Fig. 3d). The negative contribution of the mean heat advection
254 in the northern part of the domain may seem puzzling at first. However,
255 similar negative contributions are seen in the model studies by Saenko et al.
256 (2014) and de Jong et al. (2016a). We assume that this is a consequence
257 of the fact that most eddies are anticyclones, and that they tend to follow
258 a preferred path from east to west. As a result, the mean heat advection
259 term contains a mean contribution of this “train of buoyant eddies”. Once
260 the eddies have detached from the boundary current, they move westward
261 and cool along their path, which corresponds to a negative contribution to
262 the mean heat advection. As a consequence, the eddies are responsible for
263 an interior warming and the mean flow is responsible for a warming along
264 the boundary. Both are necessary to balance the heat loss that occurs over
265 the interior as well as over the boundary current. In addition, a cross sec-
266 tion of the eddy heat advection over the interior confirms that the eddies
267 transport a significant amount of heat into the interior at depths down to
268 500m (Fig. 3f).

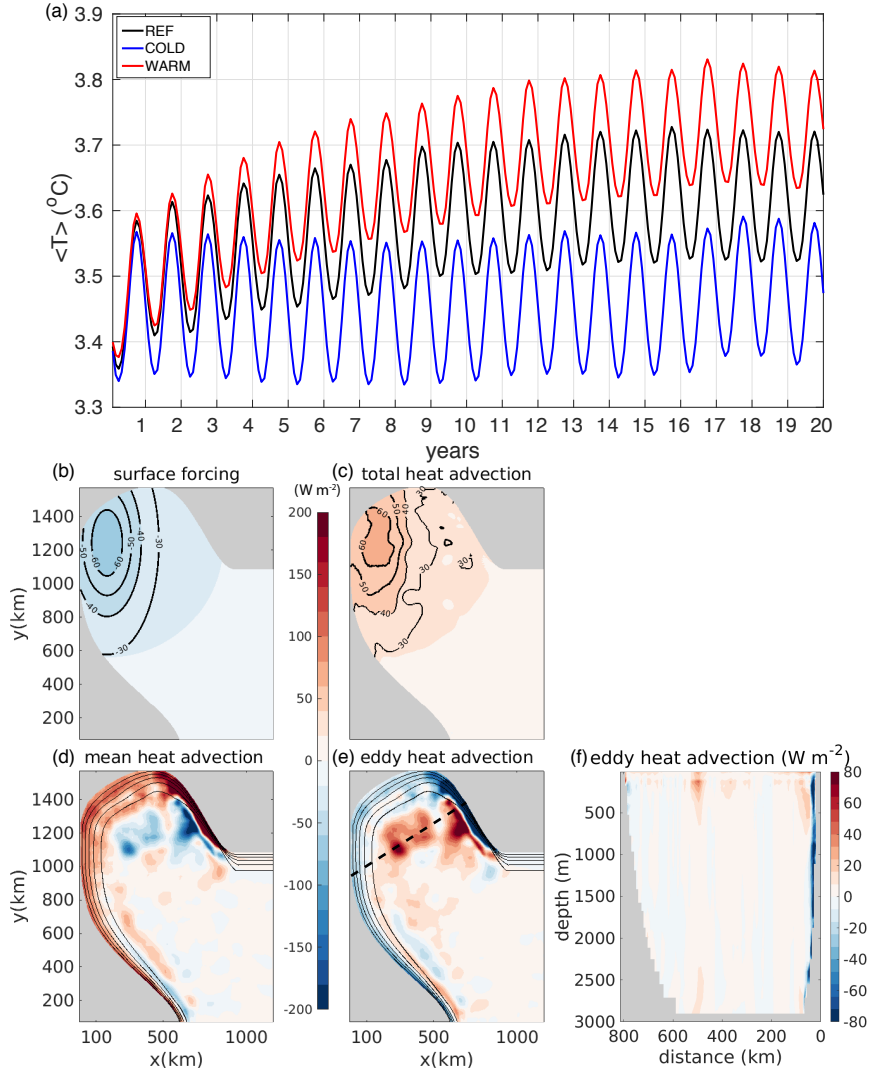


Fig. 3: (a) Timeseries of the basin-mean temperature of all simulations. (b-e) Depth-integrated terms of heat budget (in W m^{-2}) for the REF simulation (average over years 16-20): (b) surface heat flux (Q), (c) total heat advection (sum of mean and eddy component), (d) mean heat advection, $\nabla \cdot (\overline{\mathbf{U}\mathbf{T}})$, and (e) eddy heat advection, $\nabla \cdot (\overline{\mathbf{U}'\mathbf{T}'})$. Overbars denote the five year means, primes the anomalies with this respect to this mean and $\mathbf{U} = (u, v, w)$ is the velocity vector. In (d) and (e) the black contours outline the bathymetry, the contour interval is 500 m starting from the 500 m isobath. (f) Eddy heat advection (in W m^{-2}) over the section indicated by the black dashed line in (e).

269 From the above and earlier studies with a similar version of the model
 270 (Gelderloos et al., 2011) it is evident that with this set of parameters the
 271 model is able to resolve the main characteristics of the eddy field, and

272 to capture the properties of the mesoscale eddies (in particular the IRs).
273 Although with the horizontal resolution of 3.75 km the sub-mesoscale eddies
274 are not fully resolved in our model, we consider it appropriate for this
275 study since we focus on the dynamics of the downwelling in the presence of
276 mesoscale eddies.

277 **3. Deep convection and downwelling in the basin**

278 First, we examine the location and the size of the deep convection area
279 and its connection to the properties of the eddy field for the reference sim-
280 ulation. We also investigate the characteristics of the downwelling, which is
281 expected to peak in regions of high eddy activity, as discussed in [section 1](#).

282 *3.1. Properties of the mixed layer depth and eddy field*

283 We calculate the mixed layer depth (MLD), following [Katsman et al.](#)
284 (2004), as the depth at which the temperature is 0.025 °C lower than the
285 surface temperature (equivalent to a change in density of $5 \times 10^{-3} \text{ kg m}^{-3}$).
286 The black contours in [Fig. 4a](#) show the winter (February-March, FM) mean
287 patterns of the mixed layer depth (MLD) averaged over the last 5 years
288 of the reference simulation (REF). The deepest convection is found in
289 the southwestern part of the Labrador Sea, reaching depths of 1700 m.
290 Note that the deepest mixed layers are not located where the maximum
291 heat loss is applied (blue contours in [Fig. 4a](#)). A mean hydrographic sec-
292 tion across the domain in late spring (May, [Fig. 4b](#)) shows that in this
293 idealized model the convected water is found between the isopycnals of
294 $\sigma = \rho - 1000 = 28.32 - 28.40 \text{ kg m}^{-3}$. In addition, the surface layer is get-
295 ting warmer at this time suggesting the beginning of the restratification
296 phase as seen in observations ([Lilly et al., 1999](#); [Pickart and Spall, 2007](#)).
297 Overall, in REF the location and the depth of the convection area agree well
298 with observations ([Lavender et al., 2000](#); [Pickart et al., 2002](#); [Våge et al.,](#)
299 [2009](#); [Yashayaev and Loder, 2009](#)) and complex high-resolution model simu-
300 lations ([Böning et al., 2016](#)), certainly considering the idealizations applied
301 in the model.

302 In REF, IRs propagate from their formation site near the coast towards
303 the interior, as is shown in [Fig. 5a](#) by means of the relative vorticity at the
304 surface. Their signal is weaker but still evident in deeper layers ([Fig. 5b-d](#)).
305 This is in agreement with the example cross-section of an IR ([Fig. 1c](#)),
306 which displays a vertical extent of 1000-1500 m. The IRs carry buoy-
307 ant water from the boundary current into the interior Labrador Sea and

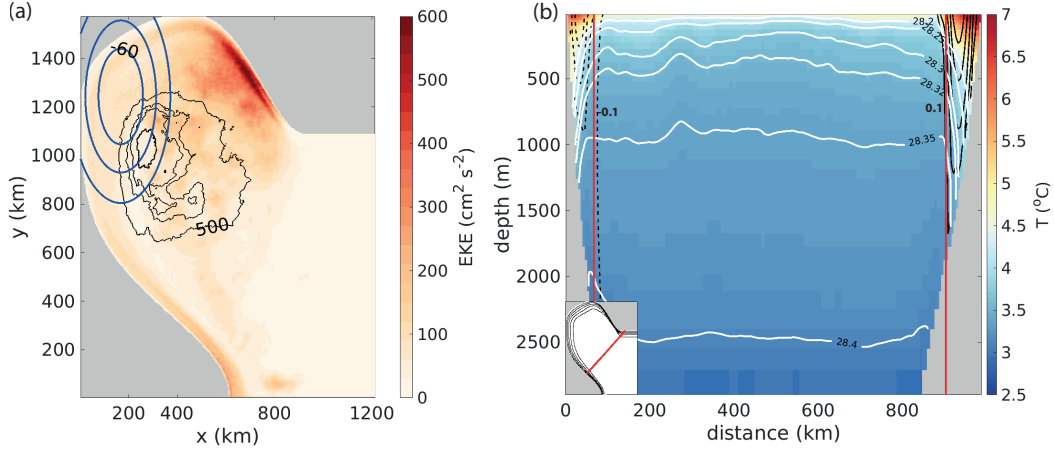


Fig. 4: (a) Mean eddy kinetic energy (EKE in $\text{cm}^2 \text{s}^{-2}$, shading) superimposed on the contours of the winter mixed layer depth (MLD in m, contour interval is 500 m) for REF. Blue contours denote the annual mean surface heat fluxes in W m^{-2} that have been applied to the simulation (contour interval is 10 W m^{-2}). (b) Late spring (May) mean temperature (shading, in $^{\circ}\text{C}$) and density $\sigma = \rho - 1000$ (in kg m^{-3} ; contour interval is 0.05 kg m^{-3}) over a section indicated by the red line in the inset figure, for REF. The section is plotted against distance from the west coast (km). Positive (negative) velocity contours are shown in black solid (dashed) lines (contour interval is 0.1 cm s^{-1}). The vertical red line indicates the limits of the boundary current based on the barotropic streamfunction. Values are averaged over years 16-20.

308 they effectively limit the extent of convection. To illustrate the extent of
 309 the impact of the IRs, we use the surface eddy kinetic energy, defined as
 310 $\text{EKE} = \frac{1}{2} (\overline{u'^2 + v'^2})$, where the overbar indicates the time averaged val-
 311 ues of the five years considered and the primes are the deviations from
 312 the 5-year mean fields (shading in Fig. 4a). The EKE has a maximum
 313 of $625 \text{ cm}^2 \text{ s}^{-2}$ near the West Greenland continental slope and fades away
 314 offshore in a tongue-like shape. Its magnitude and pattern are in quantita-
 315 tive agreement with studies that derive EKE from altimetry (Prater, 2002;
 316 Lilly et al., 2003; Brandt et al., 2004; Zhang and Yan, 2018). Enhanced
 317 EKE is also observed along the Labrador coast with maximum values of
 318 $200 \text{ cm}^2 \text{ s}^{-2}$, which is also associated with local instability of the boundary
 319 current (Brandt et al., 2004).

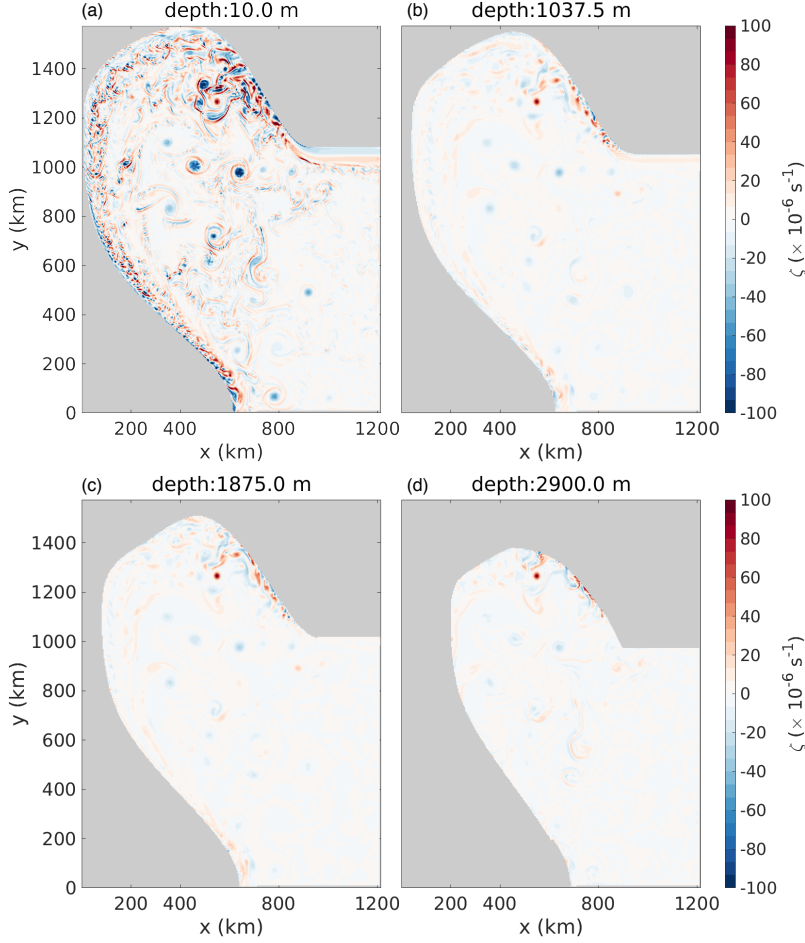


Fig. 5: Snapshot of the relative vorticity ($\zeta = \frac{\partial v}{\partial x} - \frac{\partial u}{\partial y}$, in 10^{-6} s^{-1}) for REF at the beginning of year 18 of the simulation at a depth of (a) 10.0 m, (b) 1037.5 m, (c) 1875.0 m and (d) 2900.0 m.

320 It is noteworthy that this highly idealized configuration is able to pro-
 321 duce a realistic surface EKE and mixed layer, with regard to depth, location
 322 and extent (Fig. 4a). These mixed layer properties are not prescribed, in
 323 contrast to the study by Gelderloos et al. (2011), in which a convective
 324 patch was artificially created in the domain in a similar configuration of the
 325 model. Together with Fig. 3, this indicates that the current model setup
 326 captures the physical processes that are essential to the cycle of convection
 327 and restratification in the Labrador Sea, and hence is suited for this type
 328 of process study.

329 *3.2. Vertical velocities and downwelling*

330 To analyze the downwelling in the basin, we first calculate the time-
331 mean vertical velocity integrated over the total domain and within four
332 areas (Fig. 6a). Each of these areas is characterized by different dynamics:
333 area 1 is the region where the IRs are formed, area 2 is the region where the
334 strongest heat loss is applied, area 3 is the region in the southwest part of
335 the domain where the second EKE maximum is found (Fig. 4a) and area 4
336 defines the interior, where the bottom is flat. In particular, the distinction
337 between the interior and the boundary current areas is based on a cutoff
338 value for depth (i.e. 2900m). The western edge of area 1 is defined to be
339 well downstream of the EKE maximum.

340 It appears that in this idealized model an overturning is present. The net
341 vertical transport over the total domain is downward (black line in Fig. 6b).
342 It amounts to 3.0 Sv and peaks at a depth of 1000 m.

343 The horizontal distribution of the time-mean vertical velocities at this
344 depth of maximum downward transport (i.e. 1000 m) in REF (Fig. 6c)
345 shows two regions of strong vertical velocities along the lateral boundaries:
346 one close to the steepening of the slope at the northeastern part of the
347 domain and one close to the Labrador coast. This finding that high values
348 of vertical velocity occur in a narrow area close to the lateral boundaries,
349 in particular in areas characterized by elevated surface EKE (Fig. 4a), is
350 in line with results from several idealized model studies (Spall and Pickart,
351 2001; Spall, 2004, 2010; Pedlosky and Spall, 2005) and global model studies
352 (Luo et al., 2014; Brüggemann et al., 2017; Katsman et al., 2018). The
353 outcome that the west coast of Greenland (area 1) and the Labrador coast
354 (area 3) are identified as regions of enhanced downwelling again highlights
355 the importance of the eddies for the dynamics of the Labrador Sea (see
356 Fig. 4a).

357 Fig. 6b, which shows the vertical transport as a function of depth inte-
358 grated over the full domain and the four areas, confirms that indeed the net
359 downward transport seen in the model takes place in areas 1 and 3. The
360 downwelling peaks in area 1 at a depth of 1000 m (green line in Fig. 6b) and
361 amounts to 3.4 Sv, while in area 3 it amounts to 1.0 Sv at a depth of 1525
362 m. The areas 2 and 4 are characterized by a small net upwelling despite the
363 fact that these two areas are subjected to the strongest surface heat loss.
364 Focusing on the formation area of the IRs, we next analyze the vertical ve-
365 locity over a cross section in area 1 (Fig. 6d). It is evident from this figure
366 that the mean vertical transports in the interior are very low (at a distance

367 greater than 60 km from the coast). Similarly to [Spall \(2004\)](#), the down-
368 welling is concentrated close to the boundary, while there is an upwelling
369 region farther offshore. This cell-like structure is what is expected from
370 boundary layer dynamics ([Pedlosky and Spall, 2005](#)). Overall, as shown in
371 [Fig. 6b](#), the net transport in this area is downward.

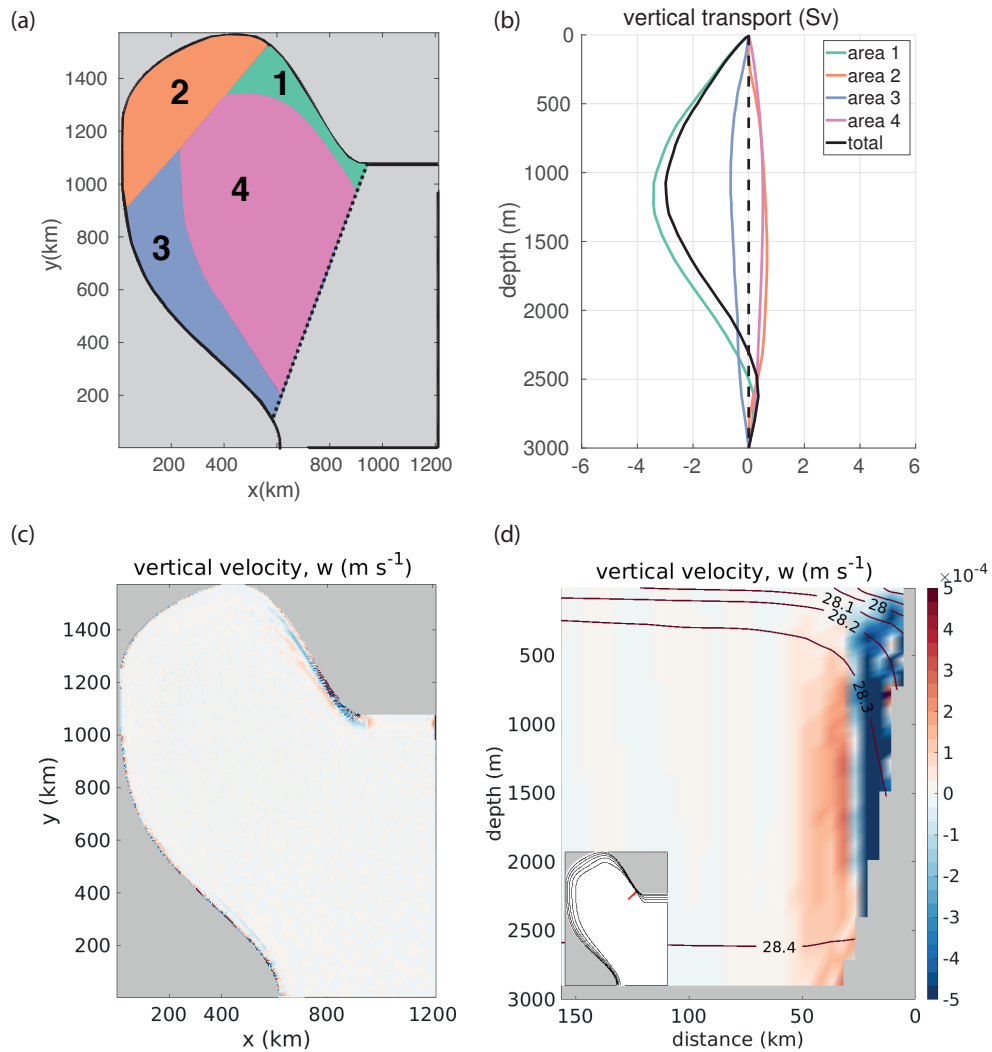


Fig. 6: (a) Definition of four areas (see text for detailed description). The total area of our interest is defined by the dashed line. (b) Vertical transport in depth space over the total domain and for the four areas (color-coded according to the map in (a)) for the REF simulation. (c-d) Vertical velocity at (c) 1000 m depth and (d) over a section across the boundary current near Greenland, indicated by the red line in the inset figure. The section is plotted against distance from the coast (km). Values are averaged over years 16-20.

372 3.3. Spreading of dense waters

373 A counterintuitive aspect that stands out from this analysis is the fact
 374 that the strongest downward motions occur at the lateral boundaries: a
 375 region associated with relatively buoyant waters rather than dense waters,

376 while at the same time it is clear from observations that dense, convected
377 waters contribute to the overturning circulation (Rhein et al., 2002; Bower
378 et al., 2009).

379 To investigate the spreading of the dense waters, we released a passive
380 tracer at the core of the convection area. The tracer is initialized with a
381 value of 1 in a cylinder of a radius 190 km and from the surface to a depth of
382 1575 m (inset in Fig. 7a) at the beginning of year 16. The maximum depth
383 for the initialization of the tracer corresponds well to the depth of the winter
384 (February-March) mixed layer of the modelled year 16. It is monitored for
385 a period of five years. After one year, the tracer is found in deeper layers
386 in the section across the domain (Fig. 7a). During winter, the tracer is
387 brought to deeper layers by convection, but by the end of the year its
388 concentration is still bounded by the isopycnals of the convected water (i.e.
389 $\sigma = 28.32 - 28.40 \text{ kg m}^{-3}$, Fig. 4b). The tracer is directly advected into the
390 boundary current at the western side of the basin (Fig. 7b-f), similarly to
391 the export route suggested by Brandt et al. (2007). However, this export
392 route mainly occurs at shallower depths ($z < 1575\text{m}$), while in deeper layers
393 the tracer also moves towards areas 1 and 2 (Fig. 7d-h, more details on the
394 evolution of the concentration of the passive tracer can be found in the movie
395 in the supplementary material). This tracer advection is clearly steered by
396 the eddy field. Once the tracer reaches area 1, which has been characterized
397 as downwelling region, it can be advected by the mean boundary current
398 (supplementary material) and exported out of the Labrador Sea following
399 the boundary current (Straneo et al., 2003).

400 This view is supported by the time evolution of the vertical distribution
401 of the tracer averaged over the four areas that is shown in Fig. 8. The
402 tracer reaches area 1 after 4 months and only at depths larger than 500 m
403 (Fig. 8a). It peaks after 13 months at a depth of 1675 m and then reduces
404 gradually over time. Although the tracer is partly initialized in area 2
405 (Fig. 8b), its concentration peaks after 14 months and at a depth of 1412.5
406 m. This provides an indication that the tracer that reaches area 1 at depth
407 is then advected by the mean boundary current towards area 2, and thereby
408 contributes in the increase of the tracer concentration in area 2. Notably, the
409 tracer peaks at shallower depths in area 2 than in area 1. This suggests that
410 it follows the isopycnals, which are rising along the boundary in all areas
411 (Fig. 4b and Fig. 7a). In area 3, the amount of tracer decreases from the
412 start and hardly penetrates deeper than the initialization depth (Fig. 8c).
413 This is in line with the view that the tracer in area 3 is predominantly

414 directly exported by the boundary current (Fig. 7c-d). Lastly, in area 4 the
415 amount of tracer reduces slowly over time (Fig. 8d).

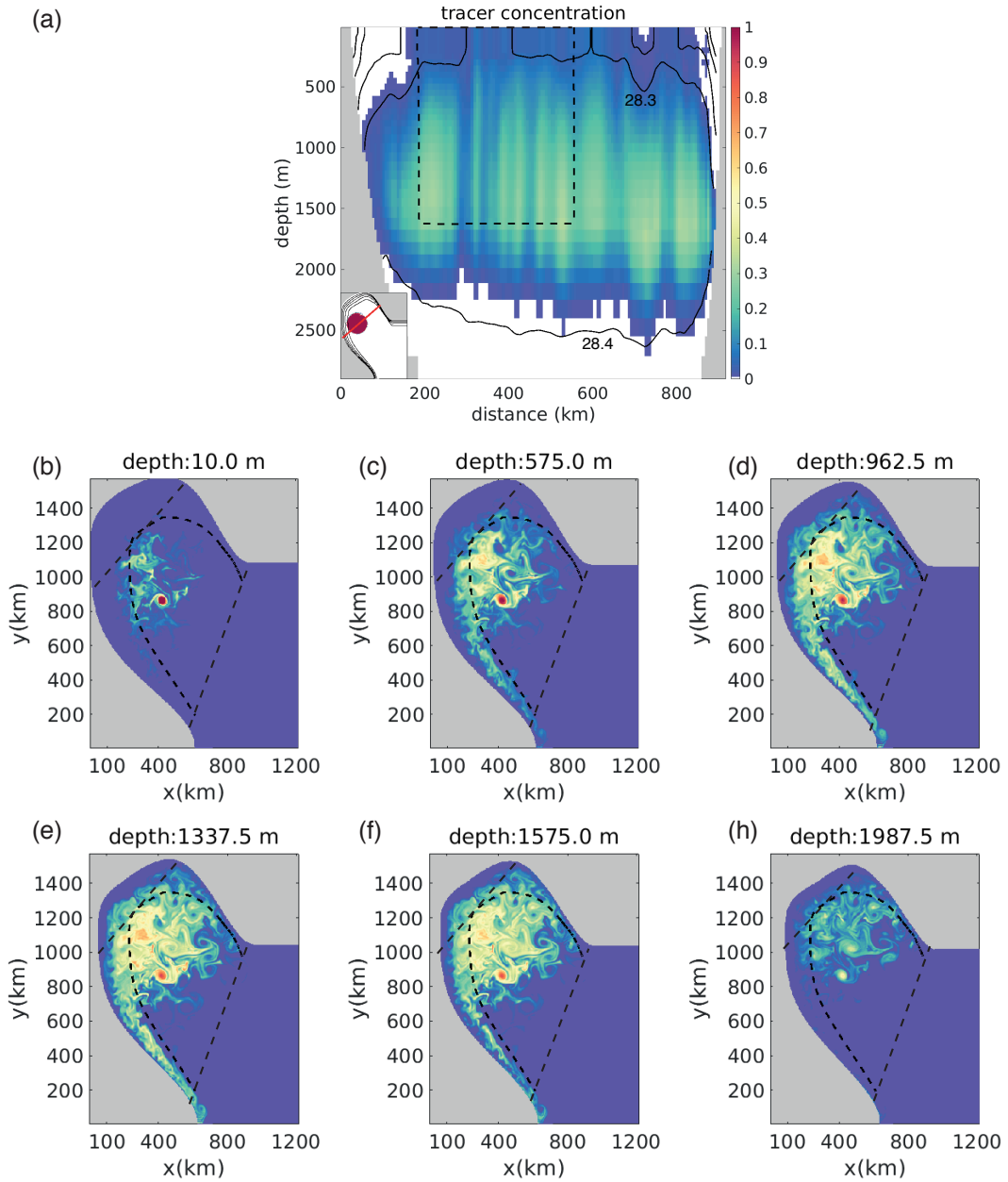


Fig. 7: (a) Cross section of the vertical distribution of the passive tracer at the end of year 16 for REF, at the section indicated by the red line in the inset figure, together with the isopycnal surfaces (in kg m^{-3} , black contours). The passive tracer is released at the beginning of year 16 over a cylinder that coincides with the convection area (dashed lines and inset figure). (b-h) Snapshots of the concentration of the passive tracer 5 months after its release at a depth of (b) 10.0 m, (c) 575.0 m, (d) 962.5 m, (e) 1337.5 m, (f) 1575.0 m and (h) 1987.5 m. Black dashed lines denote the areas defined in Fig. 6a.

416 Fig. 5 shows that the signal of the eddies extends to large depths, in line
 417 with the observational study by Lilly and Rhines (2002). A feature that
 418 stands out in Fig. 7b-h is a small area (centered at $x = 425$ km and $y = 865$
 419 km) with a peak tracer concentration that extends down to 2000m, which is
 420 tracer trapped in the core of an IR. This feature should not be mistaken for
 421 an indication that westward travelling IRs capture the dense waters. This
 422 specific IR was present in the region where the tracer was initialized, and
 423 hence the tracer was added to its core. The tracer subsequently remains
 424 captured in the eddy (see movie in the supplementary material). Never-
 425 theless, the eddies do seem to indirectly govern the tracer advection. The
 426 tracer transport towards the boundary occurs because of the strong shear
 427 that is present in the velocity field around the eddies, and is strongest close
 428 to the region where the eddies are shed.

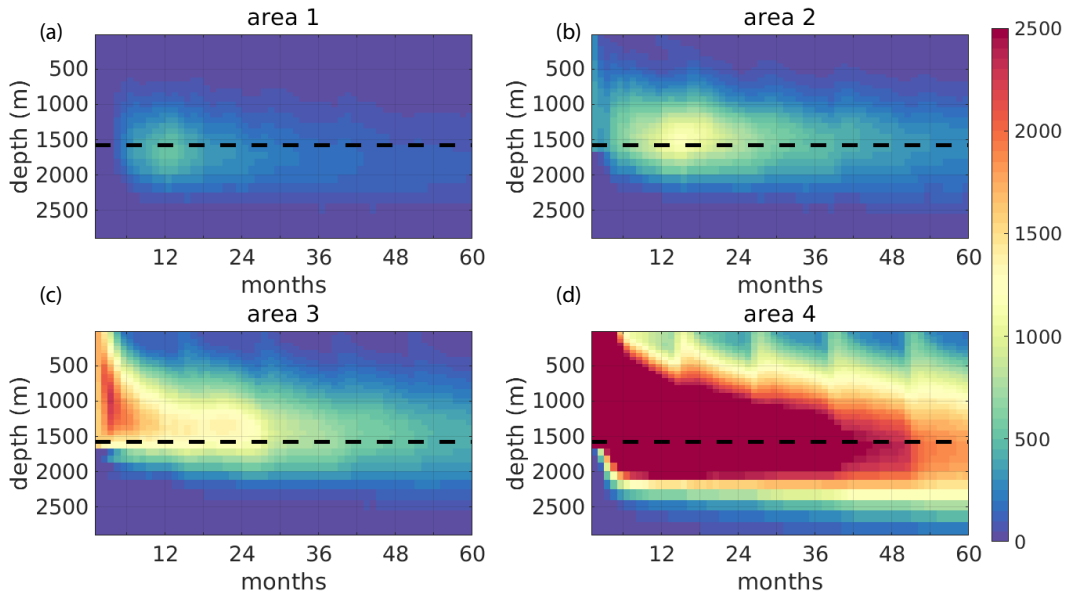


Fig. 8: Time evolution of the total amount of passive tracer in depth, integrated over (a) area 1, (b) area 2, (c) area 3 and (d) area 4 for REF. The black dashed line denotes the initial maximum depth of the tracer. The areas are defined in Fig. 6a.

429 4. Sensitivity to winter time surface heat loss

430 In this section, we assess the response of the eddies, convection and
 431 downwelling in two sensitivity simulations, in which the surface forcing is
 432 modified (see section 2.2 for details). Although the lateral eddy heat flux

433 still balances the surface heat loss when the surface heat flux is changed in
434 simulations COLD and WARM, as indicated by the regular seasonal cycle
435 in the basin mean temperature (Fig. 3), it is expected that the properties
436 of both the MLD and the EKE change. First, we focus on the response of
437 the convection and the eddy field in both simulations. Next, we assess the
438 impact of the changes in the surface forcing on the downwelling and the
439 spreading of dense waters.

440 *4.1. Response of convection and the eddy field*

441 Under the scenario of a stronger winter surface heat flux (COLD), one
442 expects that the winter mixed layer deepens, that the convection region
443 becomes wider, and that denser waters are produced. In addition, one
444 also expects that as the temperature gradient between the interior and the
445 boundary current increases due to stronger surface cooling, the eddy activity
446 is enhanced (Saenko et al., 2014; de Jong et al., 2016a). Fig. 9a and Fig. 9c
447 illustrate that when the surface heat loss is increased, EKE is indeed more
448 intense near the Greenland coast with a maximum of $750 \text{ cm}^2 \text{ s}^{-2}$, and
449 the MLD becomes deeper, reaching depths of 2100 m. In WARM, the
450 EKE is weaker (maximum value $575 \text{ cm}^2 \text{ s}^{-2}$, Fig. 9b and Fig. 9d) and the
451 reduced surface heat loss results in a much shallower mixed layer, reaching
452 depths of 960 m, and a narrower convective area. The model displays an
453 asymmetric response of the MLD to changes in the heat flux: the same
454 percentage change in the applied surface forcing results in changes of +25%
455 (Fig. 9c) and -45% (Fig. 9d) in the maximum depth of the winter mixed
456 layer. This asymmetry can be partly attributed to the stratification, which
457 increases at larger depths, and partly to the changes in the baroclinicity of
458 the boundary current and the associated eddy activity as is discussed in the
459 next paragraph.

460 Fig. 10 shows the eddy advection of heat for the three simulations. The
461 eddy component of the advective heat flux is negative for the boundary
462 current, while it is positive for the interior, once more confirming that the
463 eddies extract heat from the boundary current and transport it towards the
464 convection region. Also, the mean advection of heat in COLD and WARM
465 changes (not shown). As for REF (Fig. 3b-e), it almost cancels the eddy
466 advection. The total heat advection balances the applied surface heat loss,
467 confirming that an equilibrium is reached. Strong eddy heat fluxes originate
468 from the regions with enhanced values of EKE that have been discussed in
469 section 3 (i.e. along the Labrador coast and in particular at the steep
470 West Greenland continental slope). In COLD, not only the eddy activity is

471 stronger than in the REF case (Fig. 9c) but also the eddy advection of heat
472 from the boundary current into the interior is enhanced (Fig. 10a). Thus, as
473 the surface cooling is stronger, the restratification of the water column after
474 convection also intensifies, counteracting the deepening of the convection
475 induced by the increased surface heat loss. However, this negative feedback
476 is apparently weaker than the direct impact of the increased surface heat
477 loss on the convection depth, as the MLD deepens. In WARM, the surface
478 heat loss is smaller, but the eddy heat advection into the interior weakens
479 as well (Fig. 10c). The eddy heat advection averaged over the interior (area
480 4, Fig. 6a) amounts to 24 W m^{-2} , 28 W m^{-2} and 46 W m^{-2} for WARM,
481 REF and COLD respectively. This confirms that changes in the eddy heat
482 advection into the interior are not simply proportional to the changes in the
483 applied heat loss and that the surface heat fluxes and lateral eddy fluxes
484 combined regulate the properties of the convection.

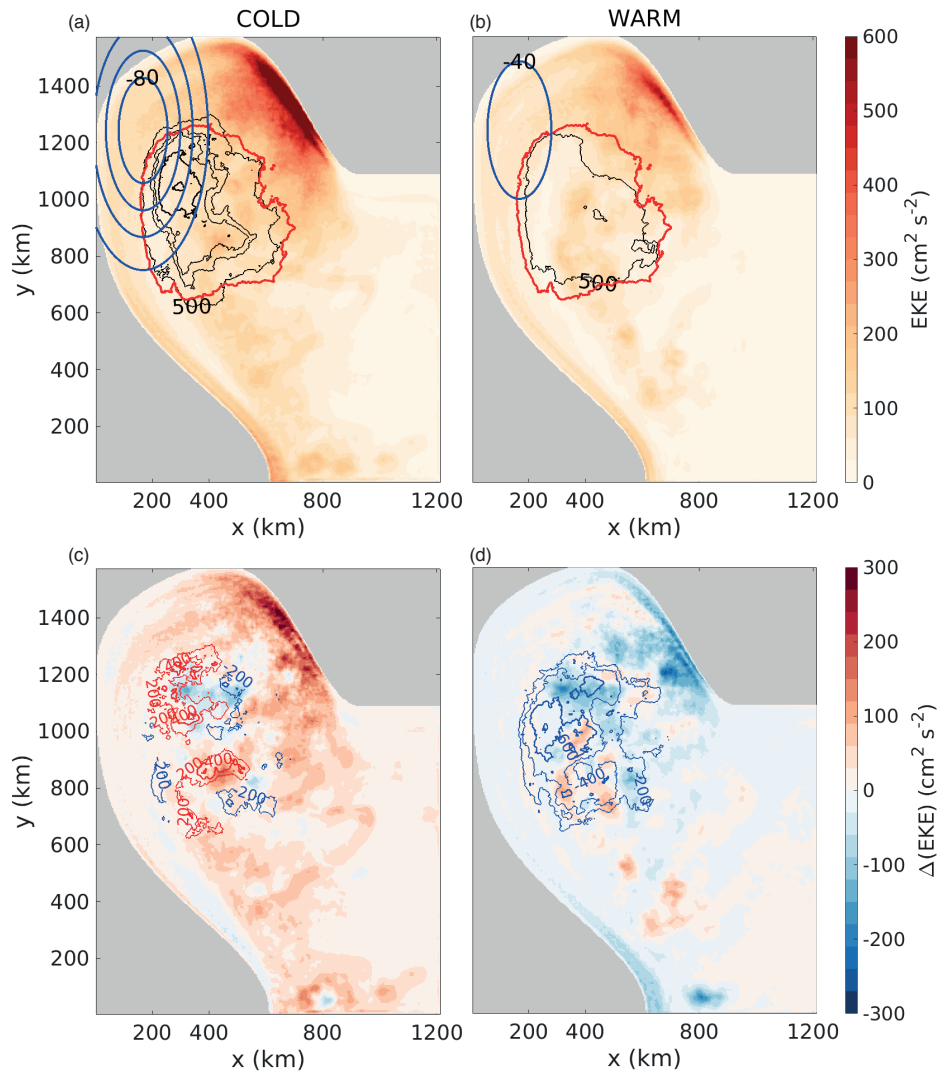


Fig. 9: (a)-(b) Wintertime (February-March) MLD and EKE, as in Fig. 4, but for the simulations (a) COLD and (b) WARM. (c)-(d) Anomalies from REF simulation of MLD (in m, contours) and EKE (in $\text{cm}^2 \text{s}^{-2}$, shading) for COLD and WARM, respectively. For comparison, the 500 m contour of the MLD for REF is shown in red in (a) and (b).

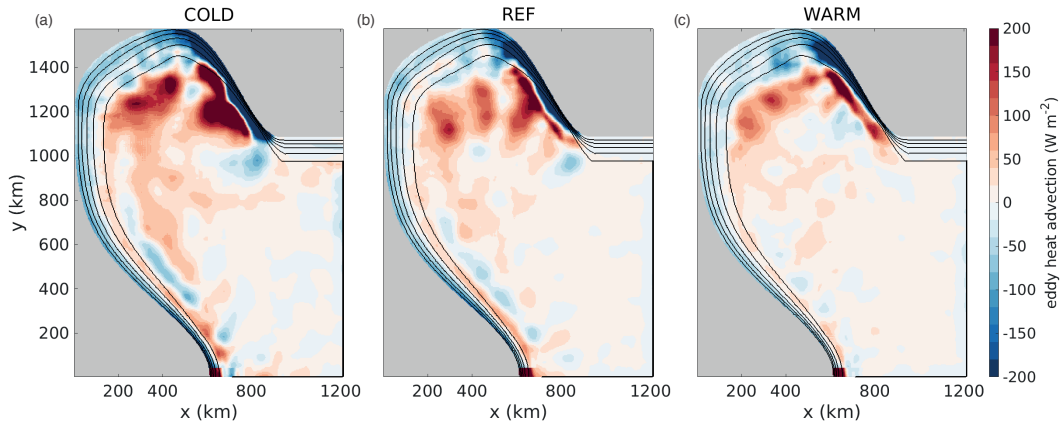


Fig. 10: Depth integrated eddy advection of heat (in W m^{-2}) for (a) WARM, (b) REF and (c) COLD. Note that panel (b) is the same as Fig. 3e and shown again here for easy comparison.

485 So clearly, along the entire West Greenland continental slope both the
 486 EKE and the eddy component of the advective heat flux are affected by the
 487 changes in the wintertime heat loss (Fig. 9c-d and Fig. 10). It is likely that
 488 this change in the eddy field will affect the dynamics of the downwelling
 489 and therefore its magnitude as well.

490 4.2. Response of the downwelling

491 Spall and Pickart (2001) and Straneo (2006b) state that the magnitude
 492 of the downwelling is controlled by the densification of the boundary cur-
 493 rent, suggesting that the magnitude of the downwelling will increase when
 494 the surface heat loss is stronger. Moreover, as shown in section 4.1, also the
 495 lateral eddy heat fluxes from the boundary current to the interior increase
 496 (Fig. 10), which is expected to further increase the downwelling. To assess
 497 how changes in the surface heat fluxes regulate the magnitude of the down-
 498 welling in the Labrador Sea, we also analyze the vertical velocities of the
 499 simulations COLD and WARM.

500 Fig. 11a shows that the time-mean vertical velocity integrated over the
 501 total domain is proportional to the applied surface heat loss. In response
 502 to an increase (decrease) of the winter heat loss by 50% compared to REF,
 503 the maximum basin-integrated downwelling increases (decreases) by 21%
 504 (-26%) or in terms of transport by +0.6 Sv (-0.8 Sv). In section 4.1, it has
 505 been shown that changes in surface heat losses influence the eddy field in the
 506 basin and this is now reflected in the magnitude of the downwelling. The
 507 downwelling in area 1 is the major contributor of the total downwelling in

508 the basin. In COLD (WARM), the surface EKE at the west Greenland con-
509 tinental slope (area 1) becomes stronger (weaker) (Fig. 9c-d) and the heat
510 loss of the boundary current increases (decreases) (Fig. 10a and Fig. 10c)
511 resulting in an increase (decrease) of the vertical transport in this region of
512 +6% (-18%).

513 Next, we investigate whether the changes in the magnitude of the down-
514 welling (Fig. 11a) are related to changes in the properties of the boundary
515 current in all simulations. Fig. 11b and Fig. 11c show the difference between
516 the velocity ($\delta V = V_{\text{outflow}} - V_{\text{inflow}}$) and the density ($\delta \rho = \rho_{\text{outflow}} - \rho_{\text{inflow}}$),
517 respectively, at the outflow and inflow for the three simulations. In all simu-
518 lations the outflow gets more barotropic. There is a slight tendency for this
519 barotropization to increase as the applied surface heat loss is stronger. The
520 density difference between the outflow and the inflow (Fig. 11c) shows that
521 the upper layer of the boundary current becomes denser along the basin
522 perimeter and that this density change increases with increasing heat loss.
523 This can be attributed to both the surface forcing and lateral eddy heat
524 advection of the boundary current (Fig. 10). In REF, the density of the
525 waters at the outflow is slightly larger than at the inflow in the lower part
526 of the boundary current ($z > 400$ m). In COLD, this difference is larger and
527 the opposite holds for WARM. This is in line with the view emerging from
528 Fig. 7 that convected waters are entrained in the boundary current. The
529 properties of the convected waters are in turn affected by the applied heat
530 loss (i.e. denser in COLD than in WARM).

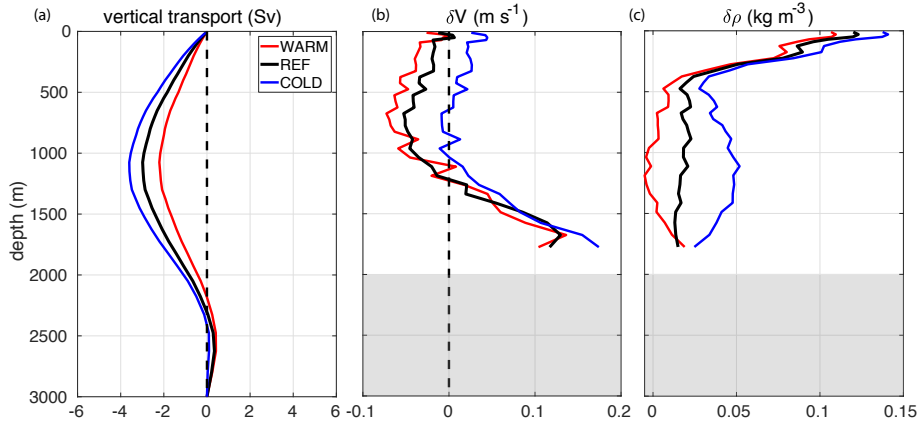


Fig. 11: (a) Vertical transport integrated horizontally over the whole domain for all the simulations. (b-c) Difference of the mean (b) velocity ($\delta V = V_{\text{outflow}} - V_{\text{inflow}}$), positive denotes an increase in the boundary current velocity and (c) density ($\delta \rho = \rho_{\text{outflow}} - \rho_{\text{inflow}}$) of the boundary current between the eastern (close to the outflow region) and western (close to the inflow region) side of the cross section shown in the inset figure of Fig. 4b. All values are averages over the 5 years considered.

531 4.3. Response of the spreading of dense waters

532 Also in WARM and COLD we performed a tracer experiment to in-
 533 vestigate the spreading of water masses that originate from the convection
 534 region. The tracer is initialized as described in section 3.3. Qualitatively,
 535 the behavior of the tracer in both WARM and COLD is the same as in REF,
 536 with a shallower pathway directly into the boundary current at the western
 537 side of the domain, and part of a deeper pathway towards Greenland (area
 538 1). In all four areas, the depth at which the maximum tracer concentration
 539 occurs increases as the surface heat loss gets stronger and vice versa when
 540 the heat loss is reduced, and this is apparently affected by the convection
 541 depth. In particular, the concentration peaks at a depth of 1800 m and
 542 1260 m for COLD and WARM in area 1, respectively (Fig. 12). Surpris-
 543 ingly, the amount of tracer peaks earlier (after 7 months) in both WARM
 544 and COLD (Fig. 12a and Fig. 12b, respectively) than in REF induced by
 545 more vigorous eddy field. We observe similar behavior in area 2 and area 3
 546 (not shown). The earlier peak in the concentration of the tracer in COLD
 547 may be related to the faster export of the convected waters than in REF.
 548 The finding that the timescale of this transport from interior towards the
 549 boundary does not display a simple relation to the heat loss emphasizes
 550 once more that complex interactions exist between convection and the eddy
 551 field.

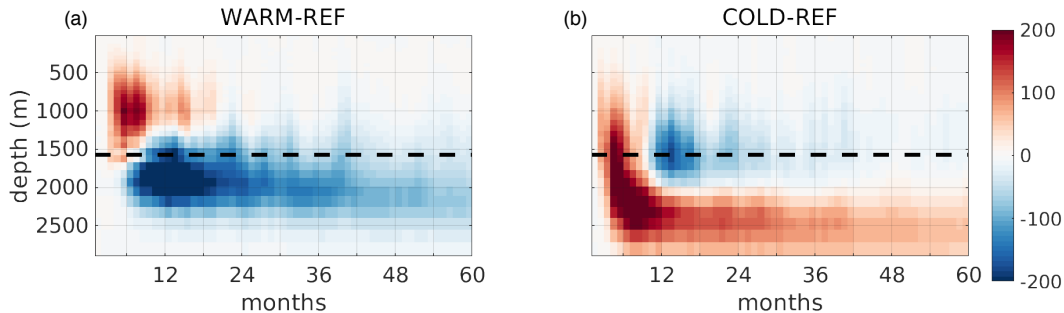


Fig. 12: Difference in the time evolution of the total amount of tracer integrated over area 1 as a function of depth for (a) WARM, (b) COLD, with respect to the REF simulation shown in Fig. 8a. The black dashed line denotes the initial maximum depth of the tracer.

552 5. Discussion

553 In the previous section, we showed that substantial downwelling is pre-
 554 dominantly appearing in areas with strong eddy activity and the magnitude
 555 of the downwelling in these eddy-rich areas is positively correlated with the
 556 magnitude of the surface heat flux. This link between the wintertime cool-
 557 ing and the overturning in the North Atlantic has been pointed out in many
 558 numerical and observational studies (e.g. Biastoch et al., 2008; Curry et al.,
 559 1998), but here we demonstrate that this link is indirect (Fig. 13).

560 As shown in this study, both the convection and the eddy field are af-
 561 fected by the changes in the surface forcing. In response to a stronger
 562 (weaker) surface winter heat loss, convection is stronger and the tempera-
 563 ture gradient between the interior and the boundary current increases (de-
 564 creases). This directly impacts the eddy field; as the temperature gradi-
 565 ent increases, the baroclinicity of the boundary current increases, and the
 566 boundary current becomes more unstable. While the generation of the
 567 eddies is known to be governed by local processes, their impacts are not
 568 restricted to their generation region since they propagate away towards the
 569 interior (Fig. 4). As a result, the associated eddy heat transport from the
 570 boundary current towards the interior strengthens (Fig. 9, Fig. 10). This
 571 increases the heat loss of the boundary current, which in turn governs the
 572 magnitude of the downwelling (Spall and Pickart, 2001; Straneo, 2006b;
 573 Katsman et al., 2018), and at the same time provides a negative feedback
 574 on the convection depth. These idealized simulations thus highlight that
 575 complex interactions between the boundary current and interior are estab-
 576 lished via the eddy activity, and in concert determine the downwelling in
 577 the basin as well as the characteristics of convection.

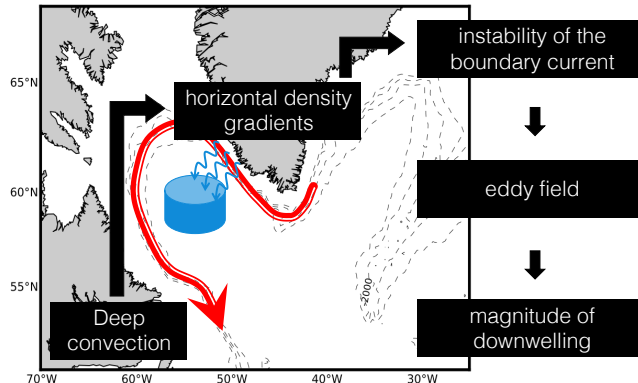


Fig. 13: Schematic showing the indirect link between convection and downwelling strength. The horizontal density gradient between the interior and the boundary current (red arrow) set by convection (blue cylinder) affects the instability of the boundary current. The eddy field and the buoyancy loss of the boundary current along the west Greenland coast govern the dynamics of the downwelling in this region.

578 In this study we focused on the Eulerian downwelling in depth space.
 579 This quantity is frequently used to describe the meridional overturning cir-
 580 culation, e.g. in the RAPID array (McCarthy et al., 2015), and in this regard
 581 it is of importance to understand the underlying physics and its sensitivity
 582 to changing surface forcing conditions. The view on the overturning based
 583 on this Eulerian downwelling differs from the view based on downwelling
 584 in density space (e.g. Mercier et al., 2015; Xu et al., 2016, 2018), which
 585 is a quantity that accounts for diapycnal processes and in particular dense
 586 water formation. While a full analysis of the watermass transformation in
 587 the basin is outside the scope of this study, we can estimate the overturning
 588 in our model using the theoretical framework outlined in Straneo (2006b).

589 In Fig. 4b one can clearly see a temperature difference between the east-
 590 ern and western side of the displayed cross-section, which reflects the fact
 591 that the boundary current loses heat along its path. That is, the isotherms
 592 (or isopycnals) rise along the path of the boundary current between the
 593 eastern and western side of the domain. The associated reduction of the
 594 density gradient between the boundary and the interior yields a decrease of
 595 the baroclinic flow and, assuming no mass transport in cross-shore direc-
 596 tion, a downward diapycnal transport in the boundary current (see Straneo
 597 (2006b) figure 1). An analysis of the changes in the boundary current be-

598 tween the inflow and the outflow region in our model simulations reveals
 599 that in all three simulations the outflow indeed gets more barotropic: the
 600 transport in the upper 1000m reduces, and the transport below that in-
 601 creases (Fig. 11b-c).

602 According to the two-layer model proposed by Straneo (2006b), the mag-
 603 nitude of the overturning w_o , i.e. the transport associated with diapycnal
 604 mass fluxes from the light to the dense layer in the boundary current, can
 605 be estimated from (Eq.17 in Straneo 2006b):

$$w_o = L \int_0^P h_2 \frac{\partial V_2}{\partial l} dl \quad (1)$$

606 where L is the width of the boundary current, V_2 the velocity of the
 607 dense lower layer, P the total perimeter of the domain and l the along-
 608 boundary coordinate. To assess w_o from our model simulations, we choose
 609 the $\sigma = 28.32 \text{ kg m}^{-3}$, isopycnal as the boundary between the light and
 610 dense layer (Fig. 4b). We define the width of the boundary current by the
 611 location of the 18 Sv streamline of the barotropic streamfunction (vertical
 612 red line in Fig. 4b), which yields $L = 66 \text{ km}$. When we average the veloc-
 613 ity of the dense layer at inflow and outflow across the boundary current,
 614 an increase of $\Delta V_2 = +0.04 \text{ m s}^{-1}$ in the velocity of the denser part of
 615 the water column is found. According to Eq. 1, this yields an overturn-
 616 ing of $w_o = 2.7 \text{ Sv}$, which is slightly smaller than the Eulerian downwelling
 617 calculated directly from the vertical velocity field in our model (i.e. 3.0 Sv).

618 The result that the changing properties of the boundary current yield
 619 an overturning does not necessarily imply that all diapycnal mixing (i.e.
 620 transformation of water masses) takes also place within the boundary, as it
 621 has been assumed in Straneo (2006b). Our tracer analysis shows that dense
 622 waters in the interior of the Labrador Sea are directly entrained in the
 623 boundary current at shallower depths at the western side of the basin. In
 624 deeper layers, the tracer moves towards the downwelling region near Green-
 625 land (Fig. 7d-h), and is then entrained in the boundary current. Thereby,
 626 the assumption that the eddy activity only yields a lateral buoyancy trans-
 627 port and no mass transport, applied in the model by Straneo (2006b), may
 628 not be correct. The pathways and the timescales by which this transport
 629 of dense waters towards the boundary occurs are complex and will be ad-
 630 dressed in more detail in a follow up study focusing on the differences and
 631 connections between the Eulerian downwelling and downwelling in density
 632 space.

633 **6. Summary and conclusions**

634 In this study we explore how changes in the surface heat fluxes affect
635 the magnitude of the downwelling, the evolution of deep ocean convection
636 in the Labrador Sea and their interplay through the eddy activity. The
637 motivation of this study stems from the need to improve our understanding
638 of the location where the downwelling takes place at high latitudes and its
639 response to changes in the forcing conditions in light of a changing climate.

640 Under the simplifications of an idealized model for the Labrador Sea
641 region, our analysis once more emphasizes that the presence of the IRs is
642 crucial to balance the heat loss over the basin (Fig. 3) and to represent the
643 restratification of the interior of the Labrador Sea (Katsman et al., 2004;
644 Hátún et al., 2007; Gelderloos et al., 2011; de Jong et al., 2016a; Kawasaki
645 and Hasumi, 2014; Saenko et al., 2014). In addition, this study once more
646 underlines that with a proper representation of the mesoscale activity in the
647 Labrador Sea the model can reproduce the winter mixed layer depths and
648 in particular the location of deep convection (Fig. 4a) seen in observations
649 (Pickart et al., 2002; Våge et al., 2009).

650 The model results show a total Eulerian downwelling in the basin of 3.0
651 Sv at a depth of 1000 m. Spall and Pickart (2001) estimated the magnitude
652 of the net downward transport in the Labrador Sea, based on observations
653 of the alongshore density variations, to be roughly of 1.0 Sv in the basin.
654 In their recent study, Holte and Straneo (2017) used horizontal velocity sec-
655 tions based on Argo floats to investigate the overturning in the Labrador
656 Sea and its variability and found a mean overturning of 0.9 ± 0.5 Sv. The
657 total net downwelling in our idealized model is in the same order of mag-
658 nitude as these observation-based estimates, albeit stronger. However, in
659 both studies, the downwelling is deduced from the large-scale hydrography
660 rather than observed directly and also the number of available observations
661 is limited.

662 The downwelling is concentrated along the lateral boundaries and not
663 where the heat loss is strongest or where convection is deepest. Moreover,
664 our analysis shows that this near-boundary vertical transport is not uniform:
665 the area where the IRs are formed contributes by far the most to the total
666 downwelling (almost 4.0 Sv of downward transport). In addition, it has
667 been shown that the time- and basin- mean downwelling is proportional
668 to the applied surface heat loss, while the downwelling near the Greenland
669 coast (area 1) displays a non-linear response to the change in heat loss.

670 This study emphasizes that a proper representation of the eddy field in

671 models is one of the key elements for representing the interplay between
672 the downwelling and convection in marginal seas at high latitudes, and
673 their responses to changing forcing conditions. The outcome that eddies
674 are a crucial element in the chain of events, determining changes in down-
675 welling in the North Atlantic Ocean and hence changes in the strength of the
676 AMOC, obviously raises the question if climate-change scenarios for AMOC
677 changes based on coarse, non-eddy resolving climate models can properly
678 represent the physical processes at hand. A first study that addresses this
679 subject (Katsman et al., 2018) showed that while also in complex models
680 the downwelling occurs near the boundary, the processes thought to govern
681 the downwelling are not well represented in the coarse ocean model that
682 was studied. An obvious next step is to carefully evaluate the response of
683 the downwelling to changing forcing conditions in such coarse resolution
684 climate models.

685 Acknowledgments

686 We kindly acknowledge the insightful comments and suggestions of three
687 anonymous reviewers. S. Georgiou, C.G. van der Boog, N. Brüggemann and
688 S.L. Ypma were supported by the Netherlands Organisation for Scientific
689 Research (NWO) via VIDI grant 864.13.011 awarded to C. A. Katsman.
690 N. Brüggemann was also partially funded by the Collaborative Research
691 Centre TRR 181. This paper is a contribution to the project S2 (Improved
692 parameterisations and numerics in climate models) of the Collaborative Re-
693 search Centre TRR 181 “Energy Transfer in Atmosphere and Ocean” funded
694 by the Deutsche Forschungsgemeinschaft (DFG, German Research Founda-
695 tion) - Projektnummer 274762653. The model data analyzed in the current
696 study are available from the corresponding author on request.

697 References

- 698 Belkin, I.M., Levitus, S., Antonov, J., Malmberg, S.A., 1998. “Great Salinity Anoma-
699 lies” in the North Atlantic. *Progress in Oceanography* 41, 1 – 68. doi:[10.1016/
700 S0079-6611\(98\)00015-9](https://doi.org/10.1016/S0079-6611(98)00015-9).
- 701 Biastoch, A., Böning, C.W., Getzlaff, J., Molines, J.M., Madec, G., 2008. Causes of
702 Interannual–Decadal Variability in the Meridional Overturning Circulation of the Mid-
703 latitude North Atlantic Ocean. *Journal of Climate* 21, 6599–6615. doi:[10.1175/
704 2008JCLI2404.1](https://doi.org/10.1175/2008JCLI2404.1).
- 705 Böning, C.W., Behrens, E., Biastoch, A., Getzlaff, K., Bamber, J.L., 2016. Emerging
706 impact of Greenland meltwater on deepwater formation in the North Atlantic Ocean.
707 *Nature Geoscience* 9, 523–527. doi:[10.1038/ngeo2740](https://doi.org/10.1038/ngeo2740).

- 708 Bower, A.S., Lozier, M.S., Gary, S.F., Böning, C.W., 2009. Interior pathways of the
709 North Atlantic meridional overturning circulation. *Nature* 459, 243–247. doi:[10.1038/nature07979](https://doi.org/10.1038/nature07979).
710
- 711 Bracco, A., Pedlosky, J., Pickart, R.S., 2008. Eddy Formation near the West Coast
712 of Greenland. *Journal of Physical Oceanography* 38, 1992–2002. doi:[10.1175/2008JP03669.1](https://doi.org/10.1175/2008JP03669.1).
713
- 714 Brandt, P., Funk, A., Czeschel, L., Eden, C., Böning, C.W., 2007. Ventilation and
715 Transformation of Labrador Sea Water and Its Rapid Export in the Deep Labrador
716 Current. *Journal of Physical Oceanography* 37, 946–961. doi:[10.1175/JP03044.1](https://doi.org/10.1175/JP03044.1).
717
- 718 Brandt, P., Schott, F.A., Funk, A., Martins, C.S., 2004. Seasonal to interannual variability
719 of the eddy field in the Labrador Sea from satellite altimetry. *Journal of Geophysical
720 Research* 109, C02028. doi:[10.1029/2002JC001551](https://doi.org/10.1029/2002JC001551).
721
- 722 Brüggemann, N., Katsman, C.A., Dijkstra, H.A., 2017. On the vorticity dynamics of the
723 downwelling branch of the AMOC, in: *CLIVAR Exchanges Special Issue: CLIVAR
724 Open Science Conference Award Winners*, pp. 10–12.
725
- 726 Chanut, J., Barnier, B., Large, W., Debreu, L., Penduff, T., Molines, J.M., Mathiot, P.,
727 2008. Mesoscale Eddies in the Labrador Sea and Their Contribution to Convection
728 and Restratification. *Journal of Physical Oceanography* 38, 1617–1643. doi:[10.1175/2008JP03485.1](https://doi.org/10.1175/2008JP03485.1).
729
- 730 Clarke, R.A., Gascard, J.C., 1983. The Formation of the Labrador Sea Water. Part
731 I: Large-Scale Processes. *Journal of Physical Oceanography* 13, 1764–1778. doi:[10.1175/1520-0485\(1983\)013<1764:TFOLSW>2.0.CO;2](https://doi.org/10.1175/1520-0485(1983)013<1764:TFOLSW>2.0.CO;2).
732
- 733 Cunningham, S.A., Kanzow, T., Rayner, D., Baringer, M.O., Johns, W.E., Marotzke,
734 J., Longworth, H.R., Grant, E.M., Hirschi, J.J.M., Beal, L.M., Meinen, C.S., Bryden,
735 H.L., 2007. Temporal Variability of the Atlantic Meridional Overturning Circulation
736 at 26.5° N. *Science* 317, 935–938. doi:[10.1126/science.1141304](https://doi.org/10.1126/science.1141304).
737
- 738 Curry, R.G., McCartney, M.S., Joyce, T.M., 1998. Oceanic transport of subpolar climate
739 signals to mid-depth subtropical waters. *Nature* 391, 575–577. doi:[10.1038/35356](https://doi.org/10.1038/35356).
740
- 741 de Jong, M.F., Bower, A.S., Furey, H.H., 2014. Two Years of Observations of Warm-Core
742 Anticyclones in the Labrador Sea and Their Seasonal Cycle in Heat and Salt Stratifica-
743 tion. *Journal of Physical Oceanography* 44, 427–444. doi:[10.1175/JPO-D-13-070.1](https://doi.org/10.1175/JPO-D-13-070.1).
744
- 745 de Jong, M.F., Bower, A.S., Furey, H.H., 2016a. Seasonal and Interannual Variations of
746 Irminger Ring Formation and Boundary-Interior Heat Exchange in FLAME. *Journal
747 of Physical Oceanography* 46, 1717–1734. doi:[10.1175/jpo-d-15-0124.1](https://doi.org/10.1175/jpo-d-15-0124.1).
748
- 749 de Jong, M.F., de Steur, L., 2016b. Strong winter cooling over the Irminger Sea in winter
750 2014–2015, exceptional deep convection, and the emergence of anomalously low SST.
751 *Geophysical Research Letters* 43, 7106–7113. doi:[10.1002/2016GL069596](https://doi.org/10.1002/2016GL069596).
752
- 753 de Jong, M.F., Olthmans, M., Karstensen, J., de Steur, L., 2018. Deep Convection in
754 the Irminger Sea Observed with a Dense Mooring Array. *Oceanography* 31, 50–59.
755 doi:[10.5670/oceanog.2018.109](https://doi.org/10.5670/oceanog.2018.109).
756
- 757 de Jong, M.F., Van Aken, H.M., Våge, K., Pickart, R.S., 2012. Convective mixing in the
758 central Irminger Sea: 2002–2010. *Deep-Sea Research Part I: Oceanographic Research
759 Papers* 63, 36–51. doi:[10.1016/j.dsr.2012.01.003](https://doi.org/10.1016/j.dsr.2012.01.003).
760
- 761 Dickson, R., Lazier, J., Meincke, J., Rhines, P., Swift, J., 1996. Long-term coordinated
762 changes in the convective activity of the North Atlantic. *Progress in Oceanography*
763 38, 241–295. doi:[10.1016/S0079-6611\(97\)00002-5](https://doi.org/10.1016/S0079-6611(97)00002-5).

- 754 Dickson, R.R., Meincke, J., Malmberg, S.A., Lee, A.J., 1988. The “great salinity
755 anomaly” in the Northern North Atlantic 1968–1982. *Progress in Oceanography* 20,
756 103 – 151. doi:[10.1016/0079-6611\(88\)90049-3](https://doi.org/10.1016/0079-6611(88)90049-3).
- 757 Eldevik, T., Nilsen, J.E.Ø., Iovino, D., Olsson, K.A., Sandø, A.B., Drange, H., 2009.
758 Observed sources and variability of Nordic seas overflow. *Nature Geoscience* 2, 406–
759 410. doi:[10.1038/ngeo518](https://doi.org/10.1038/ngeo518).
- 760 Fratantoni, P.S., Pickart, R.S., 2007. The western north atlantic shelfbreak current
761 system in summer. *Journal of Physical Oceanography* 37, 2509–2533. doi:[10.1175/
762 JPO3123.1](https://doi.org/10.1175/JPO3123.1).
- 763 Gascard, J.C., Clarke, R.A., 1983. The Formation of Labrador Sea Water. Part 2:
764 Mesoscale and Smaller-Scale Processes. *Journal of Physical Oceanography* 13, 1779–
765 1797. doi:[10.1175/1520-0485\(1983\)013<1779:tfolsw>2.0.co;2](https://doi.org/10.1175/1520-0485(1983)013<1779:tfolsw>2.0.co;2).
- 766 Gelderloos, R., Katsman, C.A., Drijfhout, S.S., 2011. Assessing the Roles of Three Eddy
767 Types in Restratifying the Labrador Sea after Deep Convection. *Journal of Physical
768 Oceanography* 41, 2102–2119. doi:[10.1175/JPO-D-11-054.1](https://doi.org/10.1175/JPO-D-11-054.1).
- 769 Gelderloos, R., Straneo, F., Katsman, C.A., 2012. Mechanisms behind the Tempo-
770 rary Shutdown of Deep Convection in the Labrador Sea: Lessons from the Great
771 Salinity Anomaly Years 1968–71. *Journal of Climate* 25, 6743–6755. doi:[10.1175/
772 JCLI-D-11-00549.1](https://doi.org/10.1175/JCLI-D-11-00549.1).
- 773 Hátún, H., Eriksen, C.C., Rhines, P.B., 2007. Buoyant Eddies Entering the Labrador
774 Sea Observed with Gliders and Altimetry. *Journal of Physical Oceanography* 37,
775 2838–2854. doi:[10.1175/2007JPO3567.1](https://doi.org/10.1175/2007JPO3567.1).
- 776 Holte, J., Straneo, F., 2017. Seasonal Overturning of the Labrador Sea as Observed
777 by Argo Floats. *Journal of Physical Oceanography* 47, 2531–2543. doi:[10.1175/
778 JPO-D-17-0051.1](https://doi.org/10.1175/JPO-D-17-0051.1).
- 779 Johns, W.E., Baringer, M.O., Beal, L.M., Cunningham, S.A., Kanzow, T., Bryden, H.L.,
780 Hirschi, J.J.M., Marotzke, J., Meinen, C.S., Shaw, B., Curry, R., 2011. Continu-
781 ous, Array-Based Estimates of Atlantic Ocean Heat Transport at 26.5 °N. *Journal of
782 Climate* 24, 2429–2449. doi:[10.1175/2010JCLI3997.1](https://doi.org/10.1175/2010JCLI3997.1).
- 783 Kanzow, T., Cunningham, S.A., Rayner, D., Hirschi, J.J.M., Johns, W.E., Baringer,
784 M.O., Bryden, H.L., Beal, L.M., Meinen, C.S., Marotzke, J., 2007. Observed Flow
785 Compensation Associated with the MOC at 26.5 °N in the Atlantic. *Science* 317,
786 938–941. doi:[10.1126/science.1141293](https://doi.org/10.1126/science.1141293).
- 787 Katsman, C.A., Drijfhout, S.S., Dijkstra, H.A., Spall, M.A., 2018. Sinking of Dense
788 North Atlantic Waters in a Global Ocean Model: Location and Controls. *Journal of
789 Geophysical Research: Oceans*, 123, 3563–3576. doi:[10.1029/2017JC013329](https://doi.org/10.1029/2017JC013329).
- 790 Katsman, C.A., Spall, M.A., Pickart, R.S., 2004. Boundary Current Eddies and Their
791 Role in the Restratification of the Labrador Sea*. *Journal of Physical Oceanography*
792 34, 1967–1983. doi:[10.1175/1520-0485\(2004\)034<1967:BCEATR>2.0.CO;2](https://doi.org/10.1175/1520-0485(2004)034<1967:BCEATR>2.0.CO;2).
- 793 Kawasaki, T., Hasumi, H., 2014. Effect of freshwater from the West Greenland Current
794 on the winter deep convection in the Labrador Sea. *Ocean Modelling* 75, 51–64.
795 doi:[10.1016/j.ocemod.2014.01.003](https://doi.org/10.1016/j.ocemod.2014.01.003).
- 796 Kulan, N., Myers, P.G., 2009. Comparing two climatologies of the Labrador Sea: Geopo-
797 tential and isopycnal. *Atmosphere–Ocean* 47, 19–39. doi:[10.3137/OC281.2009](https://doi.org/10.3137/OC281.2009).
- 798 Lavender, K., Davis, R., Owens, W., 2000. Mid-depth recirculation observed in the
799 interior Labrador and Irminger seas by direct velocity measurements. *Nature* 407,

800 66–9. doi:[10.1038/35024048](https://doi.org/10.1038/35024048).

801 Lazier, J., Hendry, R., Clarke, A., Yashayaev, I., Rhines, P., 2002. Convection and
802 restratification in the Labrador Sea, 1990–2000. *Deep-Sea Research Part I: Oceanographic Research Papers* 49, 1819–1835. doi:[10.1016/S0967-0637\(02\)00064-X](https://doi.org/10.1016/S0967-0637(02)00064-X).

803 Lilly, J.M., Rhines, P.B., 2002. Coherent Eddies in the Labrador Sea Observed
804 from a Mooring. *Journal of Physical Oceanography* 32, 585–598. doi:[10.1175/
805 1520-0485\(2002\)032<0585:CEITLS>2.0.CO;2](https://doi.org/10.1175/1520-0485(2002)032<0585:CEITLS>2.0.CO;2).

806 Lilly, J.M., Rhines, P.B., Schott, F., Lavender, K., Lazier, J., Send, U., D’Asaro, E.,
807 2003. Observations of the Labrador Sea eddy field. *Progress in Oceanography* 59,
808 75–176. doi:[10.1016/j.pocean.2003.08.013](https://doi.org/10.1016/j.pocean.2003.08.013).

809 Lilly, J.M., Rhines, P.B., Visbeck, M., Davis, R., Lazier, J.R.N., Schott, F., Farmer, D.,
810 1999. Observing Deep Convection in the Labrador Sea during Winter 1994/95. *Journal*
811 *of Physical Oceanography* 29, 2065–2098. doi:[10.1175/1520-0485\(1999\)029<2065:
812 ODCITL>2.0.CO;2](https://doi.org/10.1175/1520-0485(1999)029<2065:ODCITL>2.0.CO;2).

813 Lozier, M.S., 2012. Overturning in the North Atlantic. *Annual Review of Marine Science*
814 4, 291–315. doi:[10.1146/annurev-marine-120710-100740](https://doi.org/10.1146/annurev-marine-120710-100740).

815 Luo, H., Bracco, A., Zhang, F., 2014. The seasonality of convective events in the Labrador
816 Sea. *J. Climate* 27, 6456–6471. doi:[10.1175/JCLI-D-14-00009.1](https://doi.org/10.1175/JCLI-D-14-00009.1).

817 Marshall, J., Adcroft, A., Hill, C., Perelman, L., Heisey, C., 1997. A finite-volume,
818 incompressible Navier Stokes model for studies of the ocean on parallel computers.
819 *Journal of Geophysical Research* 102, 5753–5766. doi:[10.1029/96JC02775](https://doi.org/10.1029/96JC02775).

820 Marshall, J., Schott, F., 1999. Open-ocean convection: Observations, theory, and models.
821 *Reviews of Geophysics* 37, 1–64. doi:[10.1029/98RG02739](https://doi.org/10.1029/98RG02739).

822 McCarthy, G., Smeed, D., Johns, W., Frajka-Williams, E., Moat, B., Rayner, D.,
823 Baringer, M., Meinen, C., Collins, J., Bryden, H., 2015. Measuring the Atlantic
824 Meridional Overturning Circulation at 26°N. *Progress in Oceanography* 130, 91 –
825 111. doi:[10.1016/j.pocean.2014.10.006](https://doi.org/10.1016/j.pocean.2014.10.006).

826 Mercier, H., Lherminier, P., Sarafanov, A., Gaillard, F., Daniault, N., Desbruyères, D.,
827 Falina, A., Ferron, B., Gourcuff, C., Huck, T., Thierry, V., 2015. Variability of the
828 meridional overturning circulation at the Greenland – Portugal OVIDE section from
829 1993 to 2010. *Progress in Oceanography* 132, 250–261. doi:[10.1016/j.pocean.2013.
830 11.001](https://doi.org/10.1016/j.pocean.2013.11.001).

831 Moore, G.W.K., Renfrew, I.A., Pickart, R.S., 2012. Spatial distribution of air-sea heat
832 fluxes over the sub-polar North Atlantic Ocean. *Geophysical Research Letters* 39.
833 doi:[10.1029/2012GL053097](https://doi.org/10.1029/2012GL053097).

834 Orlanski, I., 1976. A simple boundary condition for unbounded hyperbolic flows. *Journal*
835 *of Computational Physics* 21, 251–269. doi:[10.1016/0021-9991\(76\)90023-1](https://doi.org/10.1016/0021-9991(76)90023-1).

836 Pedlosky, J., Spall, M.A., 2005. Boundary Intensification of Vertical Velocity in a β -Plane
837 Basin. *Journal of Physical Oceanography* 35, 2487–2500. doi:[10.1175/JP02832.1](https://doi.org/10.1175/JP02832.1).

838 Pickart, R.S., Spall, M.A., 2007. Impact of Labrador Sea Convection on the North
839 Atlantic Meridional Overturning Circulation. *Journal of Physical Oceanography* 37,
840 2207–2227. doi:[10.1175/JP03178.1](https://doi.org/10.1175/JP03178.1).

841 Pickart, R.S., Torres, D.J., Clarke, R.A., 2002. Hydrography of the Labrador Sea during
842 Active Convection. *Journal of Physical Oceanography* 32, 428–457. doi:[10.1175/
843 1520-0485\(2002\)032<0428:HOTLSD>2.0.CO;2](https://doi.org/10.1175/1520-0485(2002)032<0428:HOTLSD>2.0.CO;2).

844 Prater, M.D., 2002. Eddies in the Labrador Sea as Observed by Profiling RAFOS Floats
845

846 and Remote Sensing. *Journal of Physical Oceanography* 32, 411–427. doi:[10.1175/
847 1520-0485\(2002\)032<0411:EITLSA>2.0.CO;2](https://doi.org/10.1175/1520-0485(2002)032<0411:EITLSA>2.0.CO;2).

848 Rhein, M., Fischer, J., Smethie, W.M., Smythe-Wright, D., Weiss, R.F., Mertens, C.,
849 Min, D.H., Fleischmann, U., Putzka, A., 2002. Labrador Sea Water: Pathways, CFC
850 Inventory, and Formation Rates. *Journal of Physical Oceanography* 32, 648–665.
851 doi:[10.1175/1520-0485\(2002\)032<0648:LSWPCI>2.0.CO;2](https://doi.org/10.1175/1520-0485(2002)032<0648:LSWPCI>2.0.CO;2).

852 Rykova, T., Straneo, F., Bower, A.S., 2015. Seasonal and interannual variability of
853 the West Greenland Current System in the Labrador Sea in 1993–2008. *Journal of
854 Geophysical Research: Oceans* 120, 1318–1332. doi:[10.1002/2014JC010386](https://doi.org/10.1002/2014JC010386).

855 Saenko, O.A., Dupont, F., Yang, D., Myers, P.G., Yashayaev, I., Smith, G.C., 2014. Role
856 of Resolved and Parameterized Eddies in the Labrador Sea Balance of Heat and Buoy-
857 ancy. *Journal of Physical Oceanography* 44, 3008–3032. doi:[10.1175/JPO-D-14-0041.
858 1](https://doi.org/10.1175/JPO-D-14-0041.1).

859 Spall, M.A., 2004. Boundary Currents and Watermass Transformation in Marginal Seas*.
860 *Journal of Physical Oceanography* 34, 1197–1213. doi:[10.1175/1520-0485\(2004\)
861 034<1197:BCAWTI>2.0.CO;2](https://doi.org/10.1175/1520-0485(2004)034<1197:BCAWTI>2.0.CO;2).

862 Spall, M.A., 2010. Dynamics of Downwelling in an Eddy-Resolving Convective Basin.
863 *Journal of Physical Oceanography* 40, 2341–2347. doi:[10.1175/2010JP04465.1](https://doi.org/10.1175/2010JP04465.1).

864 Spall, M.A., 2012. Influences of Precipitation on Water Mass Transformation and
865 Deep Convection. *Journal of Physical Oceanography* 42, 1684–1700. doi:[10.1175/
866 JPO-D-11-0230.1](https://doi.org/10.1175/JPO-D-11-0230.1).

867 Spall, M.A., Pickart, R.S., 2001. Where Does Dense Water Sink? A Subpolar Gyre Exam-
868 ple*. *Journal of Physical Oceanography* 31, 810–826. doi:[10.1175/1520-0485\(2001\)
869 031<0810:WDDWSA>2.0.CO;2](https://doi.org/10.1175/1520-0485(2001)031<0810:WDDWSA>2.0.CO;2).

870 Straneo, F., 2006a. Heat and Freshwater Transport through the Central Labrador Sea*.
871 *Journal of Physical Oceanography* 36, 606–628. doi:[10.1175/JPO2875.1](https://doi.org/10.1175/JPO2875.1).

872 Straneo, F., 2006b. On the Connection between Dense Water Formation, Overturning,
873 and Poleward Heat Transport in a Convective Basin*. *Journal of Physical Oceanog-
874 raphy* 36, 1822–1840. doi:[10.1175/JPO2932.1](https://doi.org/10.1175/JPO2932.1).

875 Straneo, F., Pickart, R.S., Lavender, K., 2003. Spreading of Labrador sea water:
876 an advective-diffusive study based on Lagrangian data. *Deep-Sea Research Part I-
877 Oceanographic Research Papers* 50, 701–719. doi:[10.1016/S0967-0637\(03\)00057-8](https://doi.org/10.1016/S0967-0637(03)00057-8).

878 Thomsen, S., Eden, C., Czeschel, L., 2014. Stability Analysis of the Labrador Current.
879 *Journal of Physical Oceanography* 44, 445–463. doi:[10.1175/JPO-D-13-0121.1](https://doi.org/10.1175/JPO-D-13-0121.1).

880 Våge, K., Pickart, R.S., Moore, G.W.K., Ribergaard, M.H., 2008. Winter Mixed Layer
881 Development in the Central Irminger Sea: The Effect of Strong, Intermittent Wind
882 Events. *Journal of Physical Oceanography* 38, 541–565. doi:[10.1175/2007JP03678.1](https://doi.org/10.1175/2007JP03678.1).

883 Våge, K., Pickart, R.S., Sarafanov, A., Knutsen, Ø., Mercier, H., Lherminier, P., van
884 Aken, H.M., Meincke, J., Quadfasel, D., Bacon, S., 2011. The Irminger Gyre: Circula-
885 tion, convection, and interannual variability. *Deep Sea Research Part I: Oceanographic
886 Research Papers* 58, 590–614. doi:[10.1016/j.dsr.2011.03.001](https://doi.org/10.1016/j.dsr.2011.03.001).

887 Våge, K., Pickart, R.S., Thierry, V., Reverdin, G., Lee, C.M., Petrie, B., Agnew, T.a.,
888 Wong, A., Ribergaard, M.H., 2009. Surprising return of deep convection to the
889 subpolar North Atlantic Ocean in winter 2007–2008. *Nature Geoscience* 2, 67–72.
890 doi:[10.1038/ngeo382](https://doi.org/10.1038/ngeo382).

891 Xu, X., Rhines, P.B., Chassignet, E.P., 2016. Temperature-salinity structure of the North

- 892 Atlantic circulation and associated heat and freshwater transports. *Journal of Climate*
893 29, 7723–7742. doi:[10.1175/JCLI-D-15-0798.1](https://doi.org/10.1175/JCLI-D-15-0798.1).
- 894 Xu, X., Rhines, P.B., Chassignet, E.P., 2018. On Mapping the Diapycnal Water Mass
895 Transformation of the Upper North Atlantic Ocean. *Journal of Physical Oceanography*
896 48, 2233–2258. doi:[10.1175/JPO-D-17-0223.1](https://doi.org/10.1175/JPO-D-17-0223.1).
- 897 Yashayaev, I., Bersch, M., van Aken, H.M., 2007. Spreading of the Labrador Sea Water
898 to the Irminger and Iceland basins. *Geophysical Research Letters* 34. doi:[10.1029/
899 2006GL028999](https://doi.org/10.1029/2006GL028999).
- 900 Yashayaev, I., Loder, J.W., 2009. Enhanced production of Labrador Sea Water in 2008.
901 *Geophysical Research Letters* 36. doi:[10.1029/2008GL036162](https://doi.org/10.1029/2008GL036162).
- 902 Yu, L., Jin, X., Weller, R.A., 2008. Multidecade global flux datasets from the Objectively
903 Analyzed Air-Sea Fluxes (OAFlux) Project: Latent and sensible heat fluxes, ocean
904 evaporation, and related surface meteorological variables. Technical Report. OAFlux
905 Proj. Tech. Rep. OA-2008-01, Woods Hole Oceanogr. Inst., Woods Hole, Mass. URL:
906 <http://oaflex.whoi.edu/>.
- 907 Zhang, W., Yan, X., 2018. Variability of the Labrador Sea Surface Eddy Kinetic Energy
908 Observed by Altimeter From 1993 to 2012. *Journal of Geophysical Research: Oceans*
909 123, 601–612. doi:[10.1002/2017JC013508](https://doi.org/10.1002/2017JC013508).